

Energy expression for the chemical bond  
between atoms in hydrides and oxides

YOSHIFUMI SHINZATO

Nagoya University

January 2008

## Content

<b>Chapter 1 General Introduction</b>	3
REFERENCES	7
<b>Chapter 2 Calculation Methods</b>	
2.1 Plane wave pseudopotential method	8
2.2 Energy density analysis (EDA)	9
REFERENCES	11
<b>Chapter 3 A unified approach to the analysis of the chemical bond in hydrides and hydrocarbons</b>	
3.1 Introduction	12
3.2 Calculation procedure	13
3.2.1 Geometry optimization and EDA calculation	13
3.2.2 Atomization energy	15
3.3 Result and discussion	16
3.3.1 Heat of formation and cohesive energy for binary metal hydrides and typical hydrocarbons	16
3.3.2 Hydrocarbons	18
3.3.3 Perovskite-type hydrides and binary hydrides	22
3.3.4 Metal hydrides	26
3.3.5 Complex hydrides	29
3.3.6 Atomization energy diagram for hydrides and hydrocarbons	32

3.4 Conclusion	34
REFERENCES	35
<b>Chapter 4 Analysis of the chemical bond in metal oxides based on the atomization energy concept</b>	
4.1 Introduction	37
4.2 Calculation procedure	39
4.2.1 Geometry optimization and EDA calculation	39
4.2.2 Atomization energy	40
4.3 Results and discussion	40
4.3.1 Cohesive energy for binary metal oxides	40
4.3.2 Binary metal oxides	41
4.3.3 Perovskite-type oxides	49
4.3.4 Carbides and nitrides	59
4.3.5 Atomization energy diagram for hydrides, hydrocarbons, oxides carbides and nitrides.	62
4.4 Conclusion	63
REFERENCES	66
<b>Chapter 5 General conclusion</b>	68
<b>List of Paper Related to the Present Study</b>	72
<b>Acknowledgments</b>	73

## Chapter 1 General Introduction

Nowadays, total energy calculation is so common in the field of material science. However, information of the chemical bond between atoms is still limited along the total energy calculation alone.

In 1955, Wigner and Seitz [1] predicted that if one had a great calculating machine, one might apply it to the problem of solving the Schrödinger equation for each metal and thereby obtain values for their physical quantities, such as the cohesive energy and the lattice constant. It is not clear, however, that a great deal would be gained by this. Presumably, the results would agree with experimentally determined quantities and nothing vastly new would be learned from the calculation. This prediction, made by two pioneers of solid-state physics, still appears to be true today, even though computational science has made great progress.

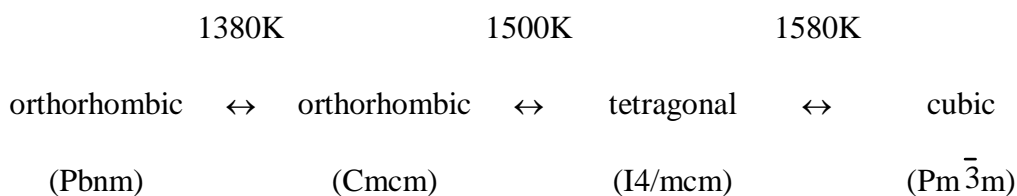
In addition, the Mulliken population analysis [2] is very common in the field of molecular orbital calculation, and the nature of the chemical bond between atoms has been defined well using the standard concept of covalent and ionic bonds. However, with this analysis it is still difficult to compare quantitatively the chemical bond strengths among a variety of materials, because, both covalent and ionic interactions are operating in most of materials. To solve this problem, the chemical bond should be estimated quantitatively in an energy scale.

Recently, Nakai proposed a new analyzing technique called energy density analysis (EDA) [3]. In this method, the total energy of a system, computed by the Kohn–Sham-type density functional theory (DFT) [4], is partitioned into atomic energy

densities, and the characteristics of the chemical bond are understood in terms of each atomic energy density instead of the total energy.

In this study, special attention is paid toward hydrides and oxides. A unified understanding of chemical bond is desired in the field of study of the hydrogen storage materials. Because many kinds of the hydrides such as complex hydrides [5], metal hydrides [6] and perovskite-type hydrides [7] have been investigated as the candidate for hydrogen storage. The bond characters are very different among them, it is important to understand the nature of the chemical bond between metal and hydrogen atoms in them in an energy scale.

Metal oxides possess a wide variety of chemical and physical properties such as superconductivity, ferroelectricity, magnetism and proton conductivity. Their phase transition is also interesting. For example, it is known that phase transition of perovskite-type oxides,  $\text{CaTiO}_3$  occurs mainly by the successive tilting or rotation of  $\text{TiO}_6$  octahedra around three O-Ti-O crystal axes [8, 9]. The sequence of the phase transition is expressed as,



However, it is still difficult to understand the mechanism of phase transition along total energy calculation alone. It is important to investigate the change of the chemical bond with the phase transition in an energy scale in order to account for the phase transition in a fundamental manner.

The purpose of this study is to calculate the atomization energy instead of using total

energy and use it for understanding the chemical bond in hydrides and oxides in an energy scale. For this purpose, the crystal structures of hydrides and oxides are optimized by plane-wave pseudopotential method [10] in order to clarify the stable structure and the EDA analysis is performed with the geometry optimized by the plane-wave pseudopotential method. The total energy of hydrides and oxides are partitioned into atomic energy density for constituent element by using EDA. Atomization energy is defined by subtracting the energy of isolated neutral atom from the atomic energy density. The advantage of using atomization energy is to know the contribution of each constituent element to the hydride or oxide formation. The atomization energy is a unique quantity that can never be obtained from the total energy calculation alone.

Following the background and the purpose as mentioned above, this paper is composed of five Chapters. The outline of each chapter is given below.

In Chapter 1, the problem of the total energy calculation and the Mulliken population analysis and the importance of analyzing the chemical bond in an energy scale are explained together with the principal purpose of this study.

In Chapter 2, two calculation methods used in the present study are explained. One is the plane-wave pseudopotential method and the other is the energy density analysis (EDA) method.

In Chapter 3, a unified approach based on the atomization energy concept is proposed for understanding the chemical bond in the hydrocarbons and hydrides such as perovskite-type hydrides, metal hydrides and complex hydrides without using the standard concept of covalent and ionic bonds.

In Chapter 4, on the basis of the atomization energy concept, the chemical bond in various binary metal oxides and perovskite-type oxides are analyzed in order to understand the chemical bond in these oxides in view of the local structure, average structure and phase transition. Other ternary oxides such as spinel-type oxides and sodium ferrites, and binary metal nitrides and carbides are treated for comparison.

In Chapter 5, a general conclusion obtained from this study is summarized.

## REFERENCES

- [1] E. P. Wigner and F. Seitz, *Solid State Phys.* 1 (1955) 97-126.
- [2] R. S. Mulliken, *J. Chem. Phys.* 23 (1953) 1833-1840.
- [3] H. Nakai, *Chem. Phys. Lett.* 363 (2002) 73-79.
- [4] W. Kohn and L. J. Sham, *Phys. Rev.* 140 (1965) A1133-A1138.
- [5] A. Ahtee, M. Ahtee, A. M. Glazer and A. W. Hewat, *Acta Cryst. B* 32 (1976) 3243-3246.
- [6] M. Ahtee, A. M. Glazer and A. W. Hewat, *Acta Cryst. B* 34 (1978) 752-758.
- [7] B. Bogdanovic and M. Schwickardi, *J. Alloys Comp.* 253-254 (1997) 1-9.
- [8] J. J. Reilly and R. H. Wiswall Jr, *Inorg. Chem.* 13 (1974) 218-222.
- [9] K. Komiya, N. Morisaku, R. Rong, Y. Takahashi, Y. Shinzato, H. Yukawa and M. Morinaga, *J. Alloys Comp.* in press. doi:10.1016/j.jallcom.2006.11.116
- [10] V. Milman, B. Winkler, J. A. White, C. J. Pickard, M. C. Payne, E. V. Akhmatukaya and R. H. Nades, *Int. J. Quant. Chem.* 77 (2000) 895-910.

## Chapter 2 Calculation Methods

### 2.1 Plane wave pseudopotential method

Geometry optimizations are employed using the first principles plane-wave pseudopotential (PW-PP) technique [1].

The main idea of PW-PP is to simplify the DFT problem by considering only valence electrons. Core electrons are excluded under the assumption that the charge densities of core electrons are not affected by any changes in the chemical environment. This approximation is well understood and it gives several advantages over DFT calculations:

- 1) The pseudopotential is much weaker in the core region than the true Coulomb potential of the nucleus, and it does not have a singularity at the position of the nucleus.
- 2) The resulting pseudo-wave functions are smooth and nodeless in the core region.
- 3) Both pseudopotentials and pseudo-wave functions can be represented efficiently by using a plane-wave basis set.
- 4) Relativistic effects, which are mainly due to core electrons, can be included in the pseudopotential.
- 5) There are fewer electronic states in the calculated electronic structure.

In the present PW-PP calculations, the effective electron-electron interaction is treated within the generalized gradient approximation (GGA) expressed as the Perdew-Wang form [2, 3]. The Vanderbilt's ultrasoft pseudopotentials are employed in the calculation [4]. The ultrasoft pseudopotential has great advantage in both accuracy and computational cost for elements with the valence 1s, 2p, 3d or 4f electrons where the norm-conserving potentials are necessarily hard [1].

The coupling with PW-PP and state-of-the-art computation for the iterative minimization of the total energy enables us to perform efficient and accurate geometry optimization [1]. For the electronic structure calculation, the self-consistent total energy in the ground state is obtained effectively by the density-mixing scheme [1, 5]. The geometry of those complex solid state materials which contain more than 10 degrees of freedom as atomic internal coordinates and cell parameters is optimized using the quasi-Newton method with the Broyden-Fletcher-Goldfarb-Shanno (BFGS) algorithm [6].

The plane-wave basis size and the number of  $\mathbf{k}$ -points using for the Brillouin zone integration should be sufficiently large with respect to the accuracy needed for the purpose of the study. The former is usually set by the kinetic energy cutoff of the plane-waves. The  $\mathbf{k}$ -points are chosen according to the mesh generated by Monkhorst and Pack's scheme [7].

## **2.2 Energy density analysis (EDA)**

The electronic structures for optimized crystal lattice of hydrides are obtained by the DFT calculations under the periodic boundary condition (PBC) using the Gaussian03 program package (Gaussian, Inc., Wallingford, CT). The adopted functional is the BLYP functional, which consists of the Slater exchange [8], the Becke (B88) exchange [9], the Vosko–Wilk–Nusair correlation [10] and the Lee–Yang–Parr correlation functionals [11]. In this study, the EDA calculations under PBC [12] are performed by linking the original code for the EDA with the Gaussian03.

Following the EDA, the atomic energy density of A atom is evaluated by,

$$E^A = E_{\text{NN}}^A + T_S^A + E_{\text{Ne}}^A + E_{\text{CLB}}^A + E_{\text{XC}}^A, \quad (1)$$

where  $E_{\text{NN}}^A$  is the nuclear-nuclear repulsion energy density,  $T_S^A$  is the non-interacting kinetic energy density,  $E_{\text{Ne}}^A$  is the nuclear-electron attraction energy density,  $E_{\text{CLB}}^A$  is the Coulomb energy density,  $E_{\text{XC}}^A$  is the exchange-correlation energy density.

In equation (1), for example,  $E_{\text{XC}}^A$  is evaluated by the partial sum for the numerical quadrature technique,

$$E_{\text{XC}}^A = \sum_g^{\text{grid}} \omega_g p_A(r_g) F_{\text{XC}}(r_g), \quad (2)$$

where  $\omega_g(r_g)$  is the weighting factor,  $p_A(r_g)$  is the partition function, and  $F_{\text{XC}}(r_g)$  is the exchange-correlation functional. The other terms in equation (1), which are evaluated by the analytical integration with the Kohn-Sham orbitals, are partitioned into their energy densities on the analogy of Mulliken population analysis [13]. For example, the Coulomb energy density for atom A,  $E_{\text{CLB}}^A$ , is evaluated by,

$$E_{\text{CLB}}^A = \frac{1}{2} \sum_{\mu \in A} (PG)_{\mu\mu}, \quad (3)$$

where  $\mathbf{P}$  is the atomic orbital-basis density matrix and the element of  $\mathbf{G}$  is given by

$$G_{\nu\mu} = \sum_{\lambda} \sum_{\sigma} P_{\lambda\sigma} \langle \chi_{\nu} \chi_{\mu} | \chi_{\sigma} \chi_{\lambda} \rangle. \quad (4)$$

Further detailed explanation of the calculation is given elsewhere [12, 14].

## REFERENCES

- [1] V. Milman, B. Winkler, J. A. White, C. J. Pickard, M. C. Payne, E. V. Akhmatkaya and R. H. Nobes, *Int. J. Quant. Chem.* 77 (2000) 895-910.
- [2] J. P. Perdew, K. Burke and Y. Wang, *Phys. Rev. B* 54 (1996) 16533-16539.
- [3] J. P. Perdew, J. A. Chevary, S. H. Vosko, K. A. Jackson, M. R. Pederson, D. J. Singh and C. Fiolhais, *Phys. Rev. B* 46 (1992) 6671-6687.
- [4] D. Vanderbilt, *Phys. Rev. B* 41 (1990) 7892-7895.
- [5] G. Kresse and J. Furthmüller, *Phys. Rev. B* 54 (1996) 11169-11186.
- [6] W. H. Press, S. A. Teukolsky, W. T. Vetterling and B. P. Flannery, *Numerical Recipes* 2nd ed., 1992.
- [7] H. J. Monkhorst and J. D. Pack, *Phys. Rev. B* 13 (1976) 5188-5192.
- [8] J. C. Slater, *Phys. Rev.* 81 (1951) 385-390.
- [9] A. D. Becke, *Phys. Rev. A* 38 (1988) 3098-3100.
- [10] S. H. Vosko, L. Wilk and M. Nusair, *Can. J. Phys.* 58 (1980) 1200-1211.
- [11] C. Lee, W. Yang and R. G. Parr, *Phys. Rev. B* 37 (1988) 785-789.
- [12] H. Nakai, Y. Kurabayashi, M. Katouda and T. Atsumi, *Chem. Phys. Lett.* 438 (2007) 132-138.
- [13] R. S. Mulliken, *J. Chem. Phys.* 23 (1955) 1833-1840.
- [14] H. Nakai, *Chem. Phys. Lett.* 363 (2002) 73-79.

## **Chapter 3 A unified approach to the analysis of the chemical bond in hydrides and hydrocarbons**

### **3.1 Introduction**

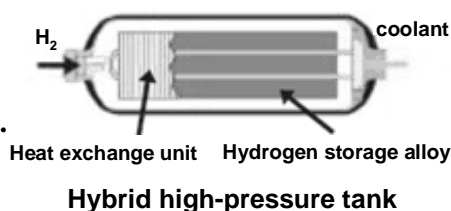
As mentioned in Chapter 1, in the field of hydrogen storage material, many kind of the hydrides such as complex hydrides [1], metal hydrides [2] and perovskite-type hydrides [3] are investigated, all of which possess very different chemical bond characters. Current status for hydrogen storage materials are shown in Fig. 3-1. For example, the conventional metal hydrides such as  $\text{TiFeH}_2$  [2],  $\text{Mg}_2\text{NiH}_4$  [4] have been developed. However, for use of the hydrogen storage material on board a vehicle, at least 3.5 mass% of hydrogen should be stored. The metal hydrides do not match this condition. To overcome this problem, complex hydrides being composed of light element such as  $\text{NaAlH}_4$  [1],  $\text{LiBH}_4$  [5] and  $\text{LiNH}_2$  [6] have been investigated. However, for these complex hydrides there are still some problems in the reversibility of hydrogenation and dehydrogenation reactions, and also in high decomposition temperature and low reaction rates [7, 8]. The total energy calculations of complex hydrides have been performed to control the enthalpy for dehydrogenation reaction [9, 10].

In this chapter, special attention is directed toward the hydrides, such as perovskite-type hydrides, complex hydrides and metal hydrides used for hydrogen storage. Also, our approach is extended to hydrocarbons such as alkane, cycloalkane, alkene, alkyne and arene. Some hydrocarbons, e.g. cyclohexane ( $\text{C}_6\text{H}_{12}$ ) and decalin ( $\text{C}_{10}\text{H}_{18}$ ), are candidate materials for hydrogen storage. [11] A unified approach is proposed on the basis of energy density analysis for understanding the nature of the

chemical bond in many crystalline hydrides and hydrocarbons.

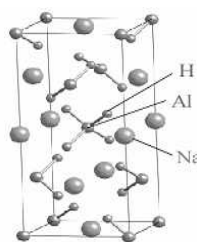
### Metal hydrides

- On-board hybrid high-pressure tank  
35MPa 70MPa
  - Ti-Cr-Mn system, Ti-Cr-V system etc.
- Stationary container
  - TiFeH<sub>2</sub> etc.



### Complex hydrides

- NaAlH<sub>4</sub> (5.5wt%)
- LiNH<sub>2</sub> (6.5wt%)
- LiBH<sub>4</sub> (18.3wt%)
- AlH<sub>3</sub> (10.1wt%)



Crystal structure of NaAlH<sub>4</sub>

#### (Problems)

- Low reaction rate.
- High decomposition temperature.
- Poor in re-hydrogenation reaction.

### Hydrocarbons

- Decahydronaphthalene (C<sub>10</sub>H<sub>18</sub>)
- Cyclohexane (C<sub>6</sub>H<sub>12</sub>)

#### (Problems)

- High reaction temperature.
- Low efficiency need to shift the equilibrium.
- Formation of the by-products (e.g. CH<sub>4</sub>).

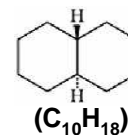


Fig. 3-1 Current status of hydrogen storage materials.

## 3.2 Calculation procedure

### 3.2.1 Geometry optimization and EDA calculation

The positions of hydrogen in hydrides are difficult to determine experimentally. Therefore, in this chapter, the crystal structures of hydrides are optimized by total energy minimization using the plane-wave pseudopotential method. For this purpose, first-principle calculations based on DFT [12] were performed with the generalized gradient approximation of Perdew et al. [13]. The implementation of DFT employed here combines a plane-wave basis set with the total energy pseudopotential method, as embodied in the CASTEP code [14]. The present calculations were based upon the ultrasoft pseudopotentials proposed by Vanderbilt [15]. The plane-wave cutoff energy

was chosen to be 380 eV, because this cutoff energy is found to achieve convergence of the total energies within 0.03 eV, as compared with the results with the cutoff energies up to 600 eV. The sampling in the reciprocal space was done with  $k$ -point grids, e.g.  $5 \times 5 \times 2$  for tetragonal NaAlH<sub>4</sub>,  $6 \times 6 \times 6$  for cubic KMgH<sub>3</sub> and  $5 \times 5 \times 9$  for monoclinic TiFeH<sub>2</sub>. The molecular structure of the hydrocarbons was optimized using the AM1 method [16].

The electronic structures for optimized crystal lattice of hydrides are obtained by the DFT calculations under the periodic boundary condition (PBC) using the Gaussian03 program package (Gaussian, Inc., Wallingford, CT). The adopted functional is the BLYP functional, which consists of the Slater exchange [17], the Becke (B88) exchange [18], the Vosko–Wilk–Nusair correlation [19] and the Lee–Yang–Parr correlation functionals [20]. The following modified Gaussian basis sets are adopted: (i) the correlation-consistent polarization plus the valence double zeta (pVDZ) basis sets of Dunning [21, 22] without d-type functions for H, Li, B, N, Na, Mg and Al, (ii) the Ahlrichs TZV basis set [23] without the outer s function for K, (iii) the Huginaga basis sets [24] without the outer s function and constructed to be double zeta class for V, Fe, Co, Ni, Rb, Zr, Nb and Pd, (iv) the 6-31G basis sets [25, 26] without the outer s function for Ti and Ca, (v) the 3-21G basis set [27] without the outer s function for Sr and (vi) the Ahlrichs pVDZ basis set [28] without the d-type function for C. In this study, the EDA calculations under PBC [29] were performed by linking the original code for the EDA with Gaussian03. Further detailed explanation of the EDA calculation is given elsewhere. [29, 30]

### 3.2.2 Atomization energy

The EDA analysis is performed with the geometry optimized by the plane-wave pseudopotential method. For binary hydrides, MH, the respective atomic energy densities of M and H are related closely to the nature of the chemical bond relevant to M and H atoms in MH. When the energy of the isolated neutral atom,  $E_M^{atom}$  (or  $E_H^{atom}$ ), is taken as a reference, the atomization energy,  $\Delta E_M$  (or  $\Delta E_H$ ), is defined as,

$$\Delta E_M = E_M^{atom} - E_M^{hydride}, \quad (1)$$

$$\Delta E_H = E_H^{atom} - E_H^{hydride}, \quad (2)$$

where  $E_M^{hydride}$  and  $E_H^{hydride}$  are the atomic energy densities for M and H in MH, respectively. In the case of ternary hydrides, (M1M2) $H_n$ ,  $\Delta E_M$  is defined as  $(\Delta E_{M1} + \Delta E_{M2})/n$ , that is the average atomization energy of M1 and M2 to be counted per hydrogen atom. Even in the other type of ternary hydride,  $\Delta E_M$  is defined in a similar way.

Then, the cohesive energy,  $E_{coh}$ , of the hydride per hydrogen atom is defined as,

$$\Delta E_M + \Delta E_H = E_{coh}. \quad (3)$$

Thus,  $\Delta E_M$  and  $\Delta E_H$  are the components of  $E_{coh}$ . So, each of the atomization energies become a measure of the chemical bonding effect of the element on the stability of the hydrides.

By setting  $y = \Delta E_H$  and  $x = \Delta E_M$ , we obtain a relation,  $y = -x + E_{coh}$ . Hence,  $E_{coh}$  is expressed as a point of intersection of this line and the y-axis at  $x = 0$ .

For hydrocarbons expressed as a chemical formula,  $C_mH_n$ ,  $\Delta E_H$  and  $\Delta E_C$  are defined as,

$$\Delta E_H = E_H^{atom} - E_H^{hydrocarbon}, \quad (4)$$

$$\Delta E_C = (E_C^{atom} - E_C^{hydrocarbon}) \times (m/n). \quad (5)$$

$\Delta E_C$  is the average atomization energy of carbon per hydrogen atom in  $C_mH_n$ . For simplicity, the sum of  $\Delta E_H$  and  $\Delta E_C$  is hereafter called the cohesive energy,  $E_{coh}$ , of the hydrocarbon per hydrogen atom, although it can exist as a solid, a liquid or a gas.

### 3.3 Result and discussion

#### 3.3.1 Heat of formation and cohesive energy for binary metal hydrides and typical hydrocarbons

First, to show the reliability of the present calculation, the heat of formation,  $\Delta H$ , for binary metal hydrides,  $MH_n$ , is calculated assuming that  $M + (n/2)H_2 \rightarrow MH_n$ , and compared with the experiment [31]. As shown in Fig. 3-2, there is good agreement between the calculated and experimental values.

The cohesive energy,  $E_{coh}$ , is a measure of the electronic stability of a hydride. As shown in Table 3-1, the difference between the calculated and experimental values for  $E_{coh}$  lies within 0.4 eV for binary metal hydrides and 0.2 eV for hydrocarbons [32]. Thus, the present calculation is performed in a reasonable manner.

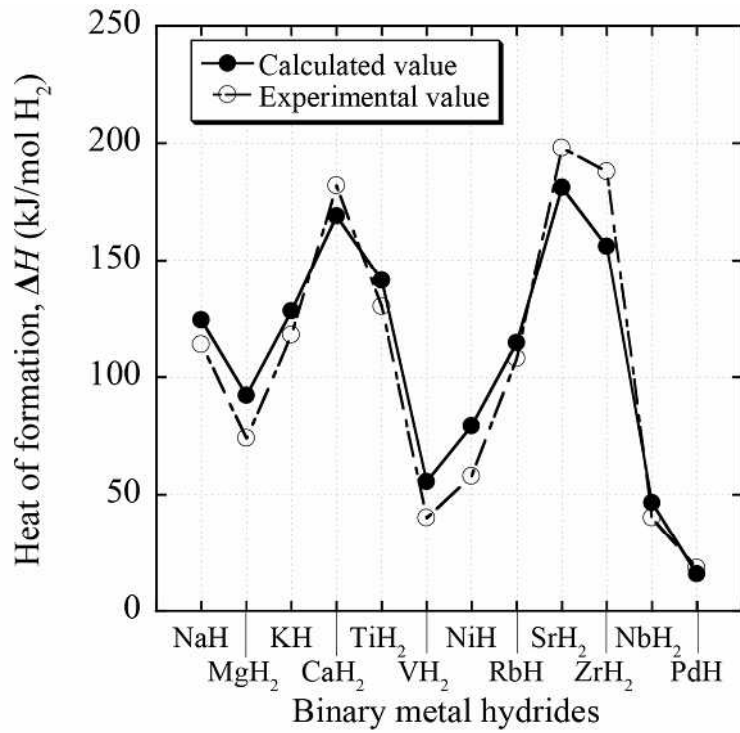


Fig. 3-2 Calculated and experimental heat of formation for binary hydrides.

Table 3-1 Calculated and experimental cohesive energies for  
(a) binary metal hydrides and (b) hydrocarbons. (units:eV)

(a) Binary metal hydrides

	$E_{coh}$ (Cal.)	$E_{coh}$ (Exp.)		$E_{coh}$ (Cal.)	$E_{coh}$ (Exp.)
NaH	4.39	3.96	TiH <sub>2</sub>	5.52	5.38
MgH <sub>2</sub>	3.34	3.41	VH <sub>2</sub>	5.08	5.13
AlH <sub>3</sub>	3.22	3.56	NiH	7.20	7.32
KH	3.38	3.78	ZrH <sub>2</sub>	6.13	6.29
CaH <sub>2</sub>	4.27	4.12	NbH <sub>2</sub>	6.48	6.20
RbH	3.34	3.64	PdH	6.17	6.58
SrH <sub>2</sub>	3.76	4.04			

(b) Hydrocarbons

	$E_{coh}$ (Calc.)	$E_{coh}$ (Exp.)		$E_{coh}$ (Calc.)	$E_{coh}$ (Exp.)
ethane, C <sub>2</sub> H <sub>6</sub>	4.95	4.86	benzene, C <sub>6</sub> H <sub>6</sub>	9.68	9.49
ethene, C <sub>2</sub> H <sub>4</sub>	5.93	5.81	toluene, C <sub>7</sub> H <sub>8</sub>	8.80	8.64
acetylene, C <sub>2</sub> H <sub>2</sub>	8.45	8.54	p-xylene, C <sub>8</sub> H <sub>10</sub>	8.26	8.14

### 3.3.2 Hydrocarbons

(a) Correlation of  $\Delta E_C$  and  $\Delta E_H$  with the ratio of carbon number to hydrogen number in  $C_2H_6$ ,  $C_2H_4$ ,  $C_2H_2$  and arene.

A simple analysis is given first for ethane ( $C_2H_6$ ), ethylene ( $C_2H_4$ ) and acetylene ( $C_2H_2$ ). As listed in Table 3-1, there is good agreement between the calculated and experimental cohesive energies. The present calculation is consistent with the previous calculation [33], since the differences in the cohesive energies between them are at most 0.16 eV for a variety of hydrocarbons.

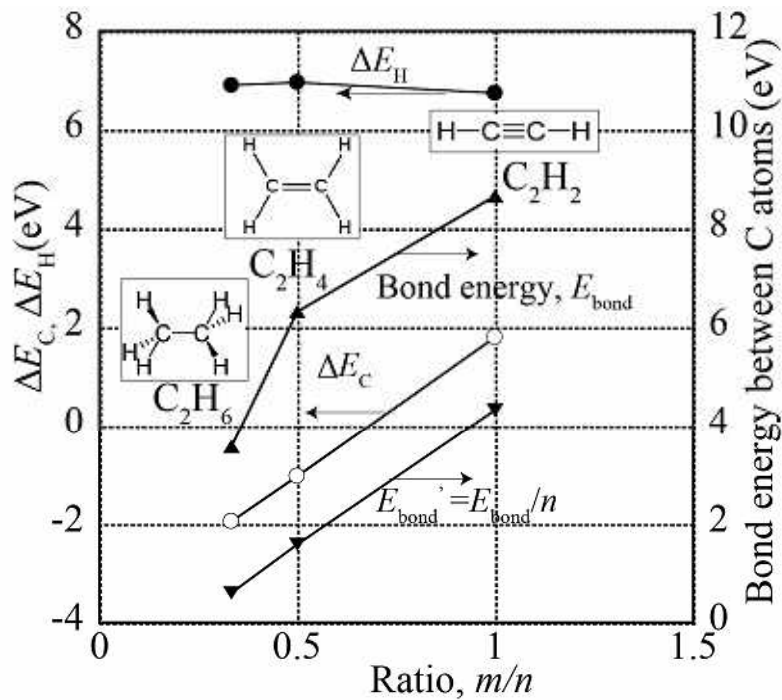


Fig. 3-3 Correlation of  $\Delta E_C$  and  $\Delta E_H$  with the ratio of carbon number to hydrogen number,  $m/n$ , in  $C_2H_6$ ,  $C_2H_4$ ,  $C_2H_2$ .

The chemical bonds between C atoms in these hydrocarbons have been treated using the concept of a single bond for C<sub>2</sub>H<sub>6</sub>, a double bond for C<sub>2</sub>H<sub>4</sub> and a triple bond for C<sub>2</sub>H<sub>2</sub>. The atomization energies for carbon,  $\Delta E_C$ , and for hydrogen,  $\Delta E_H$ , are shown in Fig. 3-3. Here,  $\Delta E_C$  is the atomization energy weighted by a factor,  $m/n$ , following Eq. (5).  $\Delta E_C$  is therefore the component of the cohesive energy partitioned into the carbon per hydrogen atom. As is evident from Fig. 3-3,  $\Delta E_C$  increases linearly with the ratio of carbon number ( $m$ ) to hydrogen number ( $n$ ),  $m/n$ , whereas  $\Delta E_H$  is nearly constant. For comparison, the bond energies between C atoms,  $E_{\text{bond}}$  [34], and its normalized values per hydrogen atom,  $E'_{\text{bond}} (= E_{\text{bond}} / n)$ , are plotted in Fig. 3-3.  $E_{\text{bond}}$  changes in the order C<sub>2</sub>H<sub>6</sub> < C<sub>2</sub>H<sub>4</sub> < C<sub>2</sub>H<sub>2</sub>, in agreement with the order of  $\Delta E_C$ . The  $E'_{\text{bond}}$  line correlates well with the  $\Delta E_C$  line, while showing a similar slope between them. Thus, the atomization energy for carbon,  $\Delta E_C$ , reflects the bond strength between C atoms in these hydrocarbons.

Next treated are the arenes, such as benzene (C<sub>6</sub>H<sub>6</sub>), toluene (C<sub>6</sub>H<sub>5</sub>CH<sub>3</sub>), naphthalene (C<sub>10</sub>H<sub>8</sub>), p-xylene (C<sub>8</sub>H<sub>10</sub>), fluorene (C<sub>13</sub>H<sub>10</sub>), phenanthrene (C<sub>14</sub>H<sub>10</sub>), pyrene (C<sub>16</sub>H<sub>10</sub>) and coronene (C<sub>24</sub>H<sub>12</sub>). Arenes have a larger  $m/n$  ratio compared with alkanes, alkenes and alkynes. As shown in Fig. 3-4,  $\Delta E_H$  values stay nearly constant and only the  $\Delta E_C$  values vary linearly with  $m/n$ . For example, in the case of benzene, it is known that the C–C bond order is about 1.67, which is stronger than the simple average of a single and a double bond owing to the resonance [34]. The C–C bond order depends on the type of the arene. Even in such an arene system,  $\Delta E_C$  varies linearly with  $m/n$ .

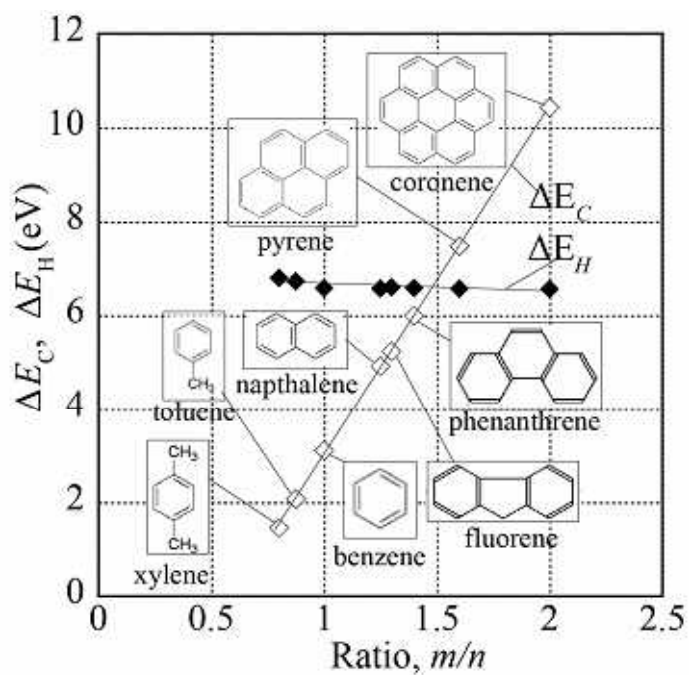


Fig. 3-4 Correlation of  $\Delta E_C$  and  $\Delta E_H$  with the ratio of carbon number to hydrogen number,  $m/n$ , in arene.

(b) Correlation of  $\Delta E_C$  and  $\Delta E_H$  with the ratio of carbon number to hydrogen number in hydrocarbon,  $C_mH_n$ .

For a variety of hydrocarbons, including alkanes, cycloalkanes, alkenes, alkynes and arenes,  $\Delta E_C$  and  $\Delta E_H$  are plotted against  $m/n$ , as shown in Fig. 3-5. There is indeed a linear relationship between  $\Delta E_C$  and  $m/n$ , and  $\Delta E_C$  is expressed approximately as,

$$\Delta E_C (\text{eV}) = 7.46 \times (m/n) - 4.46. \quad (6)$$

The correlation factor is better than 0.998. The alkynes, such as acetylene, propyne, 1-butyne and 2-butyne, deviate slightly from this relation. On the other hand, the

atomization energy for hydrogen,  $\Delta E_H$ , is a nearly constant 6.76 ( $\pm 0.22$ ) eV, irrespective of the type of hydrocarbon. So, the cohesive energy per hydrogen atom in hydrocarbons,  $E_{coh}$ , can be expressed as,

$$E_{coh} \text{ (eV)} = 7.46 \times (m/n) + 2.30. \quad (7)$$

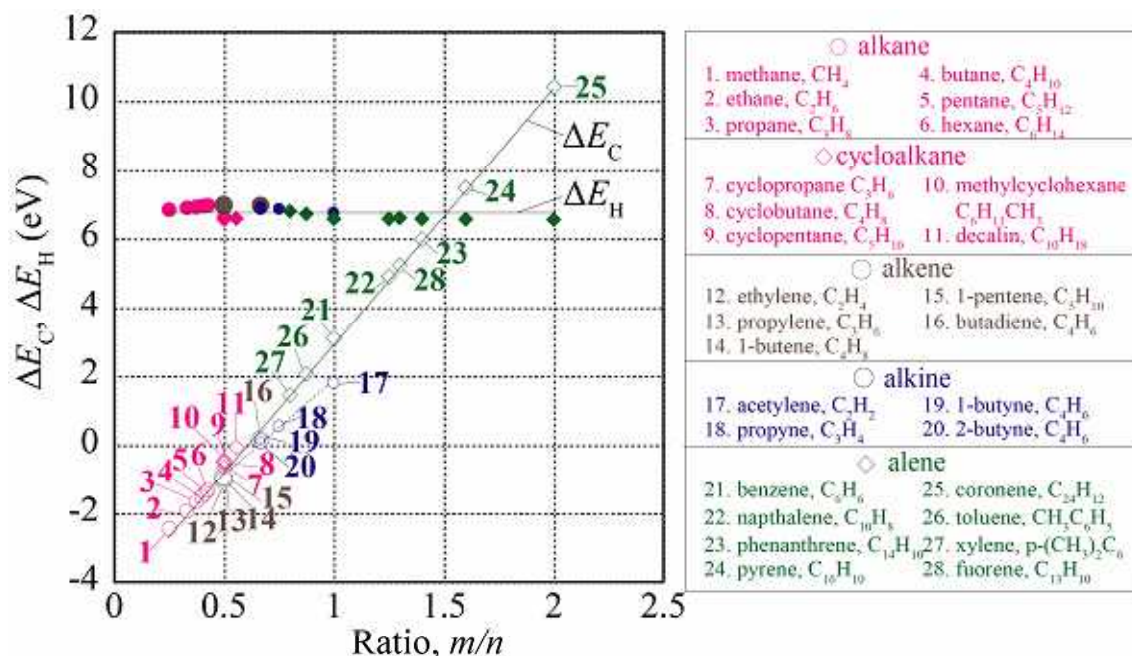


Fig. 3-5 Correlation of  $\Delta E_C$  and  $\Delta E_H$  with the ratio of carbon number to hydrogen number,  $m/n$ , in hydrocarbons,  $\text{C}_m\text{H}_n$ .

This simple relationship is satisfied in all hydrocarbons. If the cohesive energy is normalized by one molecule unit, it is expressed as  $E'_{coh} \text{ (eV)} = 7.46m + 2.30n$ . In either case, the chemical stability of  $\text{C}_m\text{H}_n$  is dependent only on  $m$  and  $n$ . It is noted here that  $m$  is not equal to the number of C–C bonds in the hydrocarbon. For example, in the case of fluorene,  $m$  is 13 and the number of C–C bonds is 15, as is evident from Fig. 3-4. Thus, by using the atomization energies,  $\Delta E_C$  and  $\Delta E_H$ , the nature of the chemical bonds

in the hydrocarbons can be understood consistently without using the concept of single or multiple bonds.

### 3.3.3 Perovskite-type hydrides and binary hydrides

#### (a) Binary hydrides

The  $\Delta E_H$  vs.  $\Delta E_M$  diagram for perovskite-type hydrides,  $M_1M_2H_3$  (e.g.  $KMgH_3$ , as shown in Fig. 3-6) is shown in Fig. 3-7 by using a symbol of solid triangle, together with some results of binary hydrides for comparison.

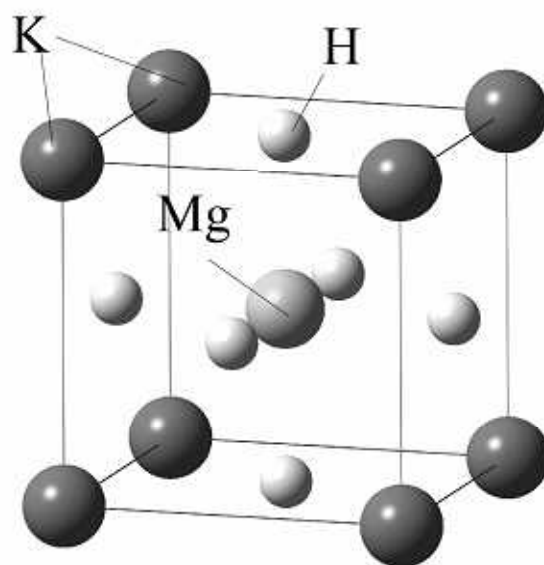


Fig. 3-6 Crystal structure of  $KMgH_3$ .

When there is resemblance in the chemical bonding state between hydrides, their locations are close to each other on the diagram. For example, the binary hydrides of transition elements (e.g.  $NiH$ ,  $PdH$ ) appear in a higher  $\Delta E_H$  region than those of more

common elements (e.g. NaH, MgH<sub>2</sub>). This indicates that transition elements could stabilize the hydrogen state remarkably in the binary hydrides probably owing to the covalent interaction between hydrogen and the transition elements. On the other hand, the binary hydrides of the more common elements have a lower  $\Delta E_H$ , probably owing to the ionic interaction mainly operating between the hydrogen and the elements.

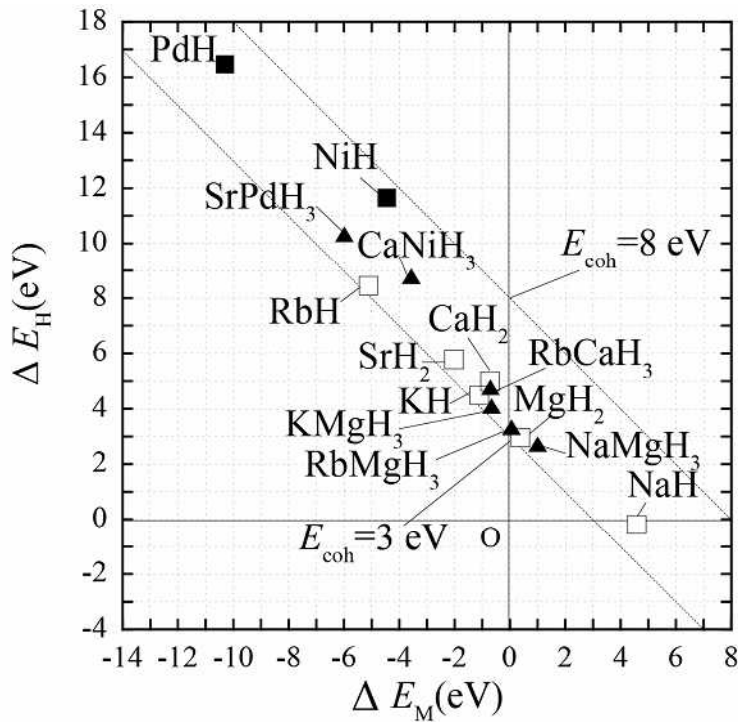


Fig. 3-7 Atomization energy diagram for perovskite-type hydrides.

Among binary alkali metal hydrides with the same crystal structure, the atomization energy for hydrogen,  $\Delta E_H$ , changes in the order NaH < KH < RbH. According to the Mulliken population analysis, the net charge on the hydrogen atom in the hydride changes in the order, NaH(-0.55) > KH(-0.71)  $\approx$  RbH(-0.71). This means that the charge transfer occurs from the metal to the hydrogen atom, and the amount of transferred charges is larger in KH and RbH than in NaH, following the

electronegativity values of 0.93 for Na, 0.82 for K and 0.82 for Rb. Thus, the hydrogen state in these hydrides is stabilized to some extent by the charge transfer, but there is still a difference in the  $\Delta E_H$  values between KH and RbH. Such a traditional analysis along the electronegativity never explains the whole feature of the atomization energy diagram expressed in an energy scale. As most materials have both ionic bond and covalent bond characteristics, only this energy-based analysis allows us to compare quantitatively the chemical bond among various materials by standing on a common ground of energy.

#### (b) Perovskite-type hydrides

For any perovskite-type hydrides,  $M_1M_2H_3$ , it is known that the M1–H and M2–H interactions are rather ionic in character, even though covalent character still remains to some extent in the M2–H bond because of the shorter M2–H distance than the M1–H one. This is the case of the perovskite-type hydrides of typical elements (e.g.,  $NaMgH_3$ ,  $RbCaH_3$ ). On the other hand, the covalent character further increases in case when M2 is a transition element. This is the case of the perovskite-type hydrides of transition elements (e.g.,  $CaNiH_3$  and  $SrPdH_3$ ). As a result,  $CaNiH_3$  and  $SrPdH_3$  possess a larger  $\Delta E_H$  than  $NaMgH_3$  and  $RbCaH_3$  as shown in Fig. 3-7. Also, perovskite-type hydrides have lower cohesive energy ( $3 \text{ eV} < E_{\text{coh}} < 6 \text{ eV}$ ) compared to perovskite-type oxides (see Fig. 4-11 in Chapter 4).

In addition, this diagram enables us to understand the chemical reaction for the formation of perovskite-type hydrides. For example, for a chemical reaction,  $\text{NaH} + \text{MgH}_2 \rightarrow \text{NaMgH}_3$ , it is found that  $\text{NaMgH}_3$  is located just in between  $\text{NaH}$  and  $\text{MgH}_2$  in this diagram. This indicates that  $\text{NaMgH}_3$  inherits the nature of the chemical bond from  $\text{NaH}$  and  $\text{MgH}_2$  to some extent. This trend is seen in the other perovskite-type hydrides as shown in Fig. 3-7.

Among the Mg-based perovskite-type hydrides,  $\text{M1MgH}_3$  ( $\text{M1} = \text{Na, K, Rb}$ ),  $\text{NaMgH}_3$  and  $\text{RbMgH}_3$  are located near  $\text{MgH}_2$  rather than  $\text{NaH}$  or  $\text{RbH}$ . The chemical bond in  $\text{NaMgH}_3$  and  $\text{RbMgH}_3$  has a resemblance to the chemical bond in  $\text{MgH}_2$  to some extent. On the other hand,  $\text{KMgH}_3$  is located near  $\text{KH}$  rather than  $\text{MgH}_2$ . So, there is a resemblance in the chemical bond between  $\text{KMgH}_3$  and  $\text{KH}$ . However, fine adjustment to the chemical bond still takes place in these hydrides.

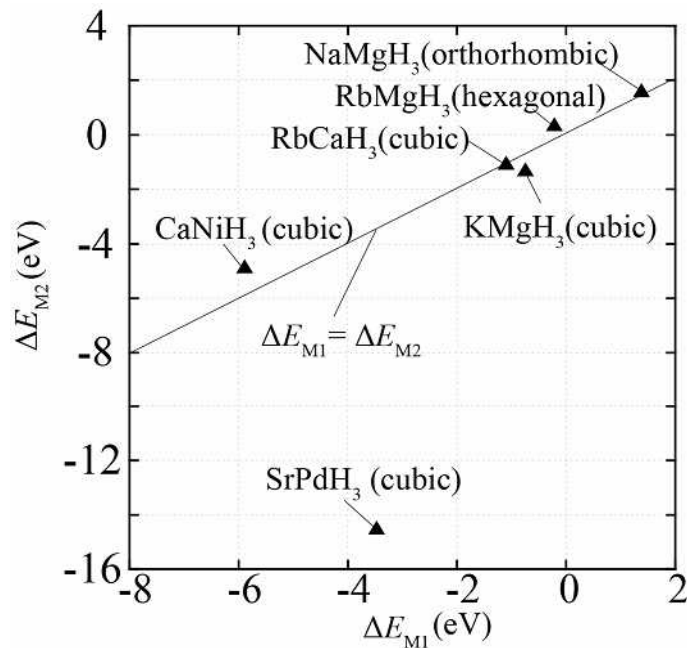


Fig. 3-8  $\Delta E_{M1}$  vs.  $\Delta E_{M2}$  diagram for perovskite-hydrides.

A  $\Delta E_{M1}$  versus  $\Delta E_{M2}$  diagram is constructed on the basis of the present calculation to understand the role of metal elements in the formation of the chemical bond in the hydride. The results are shown in Fig. 3-8.  $\Delta E_{M1}$  (or  $\Delta E_{M2}$ ) is a measure of the M1 (or M2) contribution to the cohesive energy of the perovskite-type hydride. A line showing a relation,  $\Delta E_{M1} = \Delta E_{M2}$ , is drawn in Fig. 3-8. All the perovskite-type hydrides except for  $\text{SrPdH}_3$  are located along this line. This implies that the M1 and M2 metallic states are well balanced in the perovskite-type hydrides, and their contribution to the cohesive energy is nearly equal. However, such a balance is no longer present in  $\text{SrPdH}_3$  containing Pd, where the strong covalent interaction between Pd and H atoms breaks the balance, resulting in a large, negative  $\Delta E_{\text{Pd}}$  and in a large, positive  $\Delta E_{\text{H}}$ , while showing a small, negative  $\Delta E_{\text{Sr}}$ .

### 3.3.4 Metal hydrides

For metal hydrides,  $\text{M1M2H}_n$ , where M2 is a transition metal (e.g.,  $\text{TiFeH}_2$ ), the M2–H covalent interaction is important, since H is located in the neighborhood of M2 (e.g. M2 = Fe). In the case of  $\text{Mg}_2\text{NiH}_4$ , the hydrogen atom is located in the neighborhood of Ni, and a strong covalent interaction operates there between Ni and H. In agreement with this,  $\text{Mg}_2\text{NiH}_4$  is located near to NiH rather than to  $\text{MgH}_2$  on the atomization energy diagram shown in Fig. 3-9. However, the  $\Delta E_{\text{H}}$  value is smaller in  $\text{Mg}_2\text{NiH}_4$  than in NiH, indicating that the H state is destabilized by the presence of Mg in  $\text{Mg}_2\text{NiH}_4$ . On the other hand,  $\text{TiFeH}_2$  is located well above  $\text{TiH}_2$ , so that the  $\Delta E_{\text{H}}$

value is larger in  $\text{TiFeH}_2$  than in  $\text{TiH}_2$ , indicating that the H state is further stabilized by the presence of Fe in this neighborhood rather than the neighboring Ti.

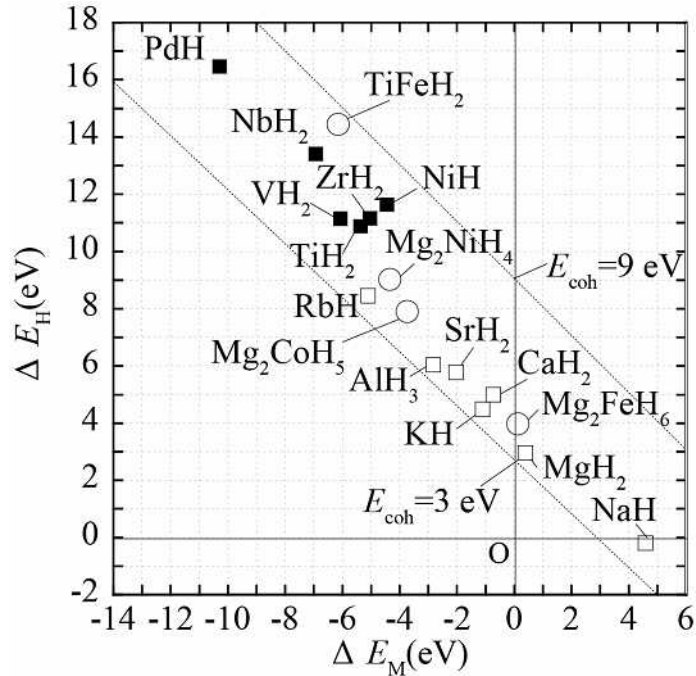


Fig. 3-9 Atomization energy diagram for metal hydrides.

$\text{Mg}_2\text{NiH}_4$  and  $\text{TiFeH}_2$  are formed by the hydrogenation of the intermetallic compounds  $\text{Mg}_2\text{Ni}$  and  $\text{TiFe}$ , respectively. Therefore, further analyses were carried out with these compounds. To understand the role of metal atoms in the bond formation, the values of  $\Delta E_{M1}$  ( $M1 = \text{Ti}$  or  $\text{Mg}$ ) and  $\Delta E_{M2}$  ( $M2 = \text{Fe}$  or  $\text{Ni}$ ) are plotted in Fig. 3-10 for  $\text{TiFe}$  and  $\text{Mg}_2\text{Ni}$ , together with the values for  $\text{TiFeH}_2$  and  $\text{Mg}_2\text{NiH}_4$ .  $\Delta E_{\text{Ti}}$  for  $\text{TiFe}$  and  $\Delta E_{\text{Mg}}$  for  $\text{Mg}_2\text{Ni}$  are negative, whereas  $\Delta E_{\text{Fe}}$  for  $\text{TiFe}$  and  $\Delta E_{\text{Ni}}$  for  $\text{Mg}_2\text{Ni}$  are positive. By hydrogenation, the atomization energy decreases in both  $M1$  and  $M2$ . However, the decrement is more remarkable in  $\Delta E_{M2}$  than in  $\Delta E_{M1}$ . This is because hydrogen exists in the neighborhood of  $M2$  and interacts strongly with  $M2$  ( $M2 = \text{Fe}$  or  $\text{Ni}$ ) in the hydrides. As a result, most of the energy of  $M2$  transfers to the hydrogen and the H state becomes

very stable, since  $\Delta E_H$  is 14.4 eV for  $\text{TiFeH}_2$  and 9.0 eV for  $\text{Mg}_2\text{NiH}_4$ . It is interesting to note that in either system of  $\text{TiFe}$  and  $\text{Mg}_2\text{Ni}$  there is a large difference between  $\Delta E_{M1}$  and  $\Delta E_{M2}$ , indicating that both  $\text{TiFe}$  and  $\text{Mg}_2\text{Ni}$  intermetallic compounds have a strong chemical bond between the M1 and M2 atoms. This is a reason why the hydrogenation and dehydrogenation reactions take place smoothly without changing the alloy compositions. Thus, this approach can clarify the role of the constituent elements in the hydrides.

It is apparent from Fig. 3-9 that both  $\Delta E_H$  and  $E_{\text{coh}}$  change in the order  $\text{Mg}_2\text{FeH}_6 < \text{Mg}_2\text{CoH}_5 < \text{Mg}_2\text{NiH}_4 < \text{VH}_2 < \text{TiFeH}_2$ . The hydrogen storage alloys of interest (e.g.,  $\text{TiFe}$  and body-centered cubic V alloys) tend to form chemically stable

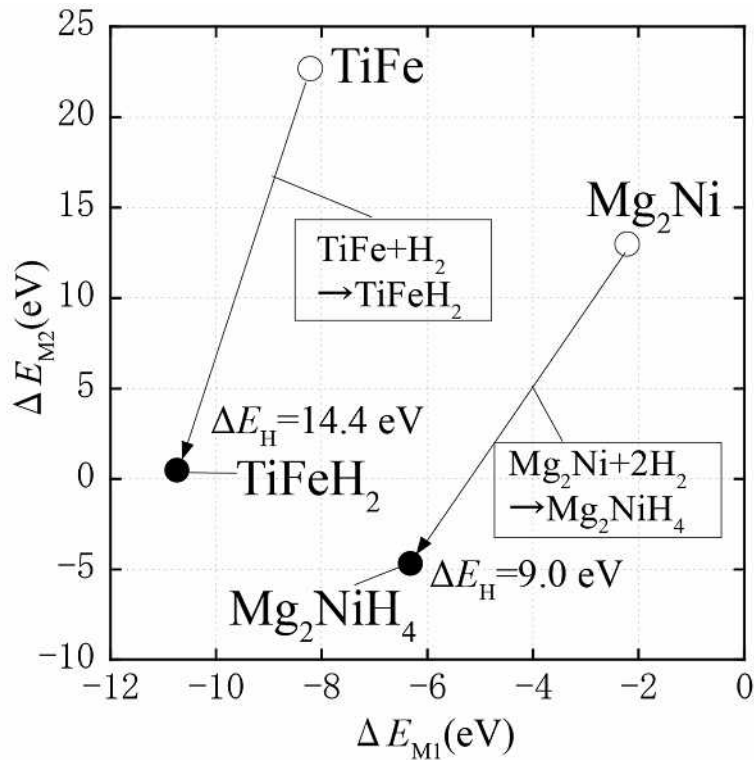


Fig. 3-10  $\Delta E_{M1}$  vs.  $\Delta E_{M2}$  diagram for  $\text{TiFeH}_2$  and  $\text{Mg}_2\text{NiH}_4$ .

hydrides with large  $\Delta E_H$  and  $E_{coh}$ .

It is interesting to note that  $TiFeH_2$ , which desorbs and absorbs hydrogen at room temperature, has the largest cohesive energy, 8.3 eV, among the metal hydrides.

For  $TiFeH_2$ , there are four sites for hydrogen atom, 1a, 1c, 1g and 1e site. The atomization energies for hydrogen atom at the 1a, 1c, 1g and 1e sites are 14.3, 13.5, 14.4 and 15.5 eV, respectively. Hydrogen state at the 1e site is most stable among four hydrogen sites in  $TiFeH_2$ . This is interpreted as due to sharing effect and average Fe-H distance. All hydrogen atoms in  $TiFeH_2$  are shared by corner. Hydrogen atom at the 1e site is shared by four Fe atoms. On the other hand, for the 1a, 1c, 1g sites, are shared by two Fe atoms. Also, for the 1a, 1c, 1g sites, hydrogen state is stabilized with decreasing average Fe-H distance. Thus, hydrogen state in  $TiFeH_2$  reflects the local atomic arrangement.

### 3.3.5 Complex hydrides

For complex hydrides,  $M_1M_2H_n$  (e.g.  $NaAlH_4$ , as shown in Fig. 3-11), it is known that strong covalent interactions are operating between H and M2 (e.g.,  $M_2 = Al$ ) to form complex ions,  $(M_2H_n)^{-1}$  (e.g.,  $(AlH_4)^{-}$ ), and that ionic interactions are operating between the complex ion and the M1 cation (e.g.,  $Na^+$ ) [35].

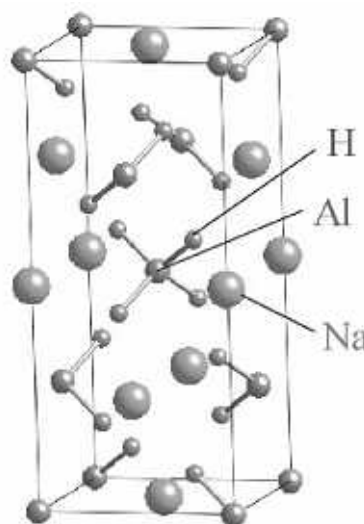


Fig. 3-11 Crystal structure of  $NaAlH_4$ .

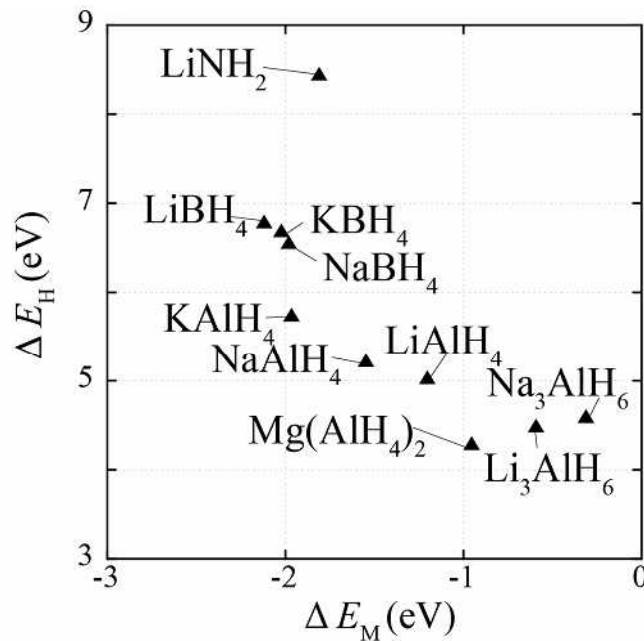


Fig. 3-12 Atomization energy diagram for complex hydrides.

As shown in Fig. 3-12, complex hydrides are located in a narrow and small  $\Delta E_M$  range ( $-2.2 \text{ eV} < \Delta E_M < -0.3 \text{ eV}$ ), but in a wide  $\Delta E_H$  range (4.2–8.5 eV).  $\Delta E_H$  changes in the order  $\text{Mg}(\text{AlH}_4)_2 < \text{M1AlH}_4$  ( $\text{M1} = \text{Li, Na, K}$ )  $< \text{M1BH}_4$  ( $\text{M1} = \text{Li, Na, K}$ )  $< \text{LiNH}_2$ . The cohesive energy,  $E_{\text{coh}}$ , changes in the same order. Thus the H state is stabilized well in compensation for the destabilized M state.

In particular, as shown in Fig. 3-13, the destabilization of the M2 state contributes mainly to the stabilization of the H state by forming the strong covalent bond between M2 and H atoms. As shown in Fig. 3-14,  $\Delta E_{\text{M1}}$  is either positive or negative, indicating that the ionic interaction between the  $(\text{M2H}_n)$  complex ion and M1 cation is not so strong as the M2-H covalent interaction. So, there is not any clear correlation between  $\Delta E_{\text{M1}}$  and  $\Delta E_{\text{M2}}$ . For  $\text{M1AlH}_4$  and  $\text{M1BH}_4$ , where M1 is the 1A group element,  $\Delta E_{\text{M1}}$  changes in the order,  $\text{K} < \text{Na} < \text{Li}$ , following the order of elements in periodic table.

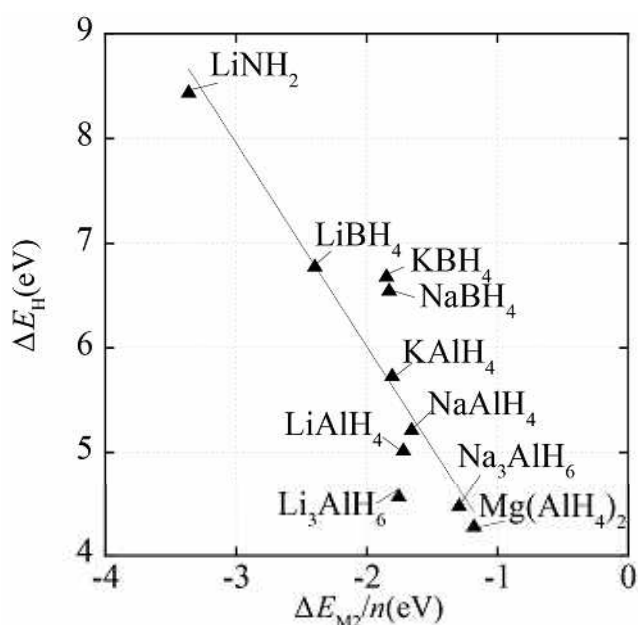


Fig. 3-13  $\Delta E_{M2}/n$  vs.  $\Delta E_H$  diagram for complex hydrides.  $n$  is the number of hydrogen atoms in the chemical formula.

In the case of alante (Al)-type complex hydrides, the magnitude of  $\Delta E_H$  changes in the order  $\text{Mg}(\text{AlH}_4)_2 < \text{LiAlH}_4 < \text{NaAlH}_4 < \text{KAlH}_4$ , as shown in Fig. 3-12. Hence, the H state in  $\text{Mg}(\text{AlH}_4)_2$  is the least stable among them, as is found experimentally [36].

In addition, the coordination number effect can be understood by using the atomization energy diagram. In  $\text{Na}_3\text{AlH}_6$  (or  $\text{Li}_3\text{AlH}_6$ ), an Al atom is surrounded by six hydrogen atoms, whereas in  $\text{NaAlH}_4$  (or  $\text{LiAlH}_4$ ) an Al atom is surrounded by four hydrogen atoms. As shown in Fig. 3-12,  $\Delta E_H$  is lower in  $\text{Na}_3\text{AlH}_6$  (or  $\text{Li}_3\text{AlH}_6$ ) than in  $\text{NaAlH}_4$  (or  $\text{LiAlH}_4$ ). Thus, the H state is less stable in  $\text{Na}_3\text{AlH}_6$  (or  $\text{Li}_3\text{AlH}_6$ ) than in  $\text{NaAlH}_4$  (or  $\text{LiAlH}_4$ ), as might be expected from the coordination number.

Also, there is a trend that  $\Delta E_H$  increases with decreasing average Al–H distance; for example, it is 0.161 nm for  $\text{NaAlH}_4$  and 0.175 nm for  $\text{Na}_3\text{AlH}_6$ . Thus, local structure such as the interatomic distance and the coordination number affects the atomization

energies.

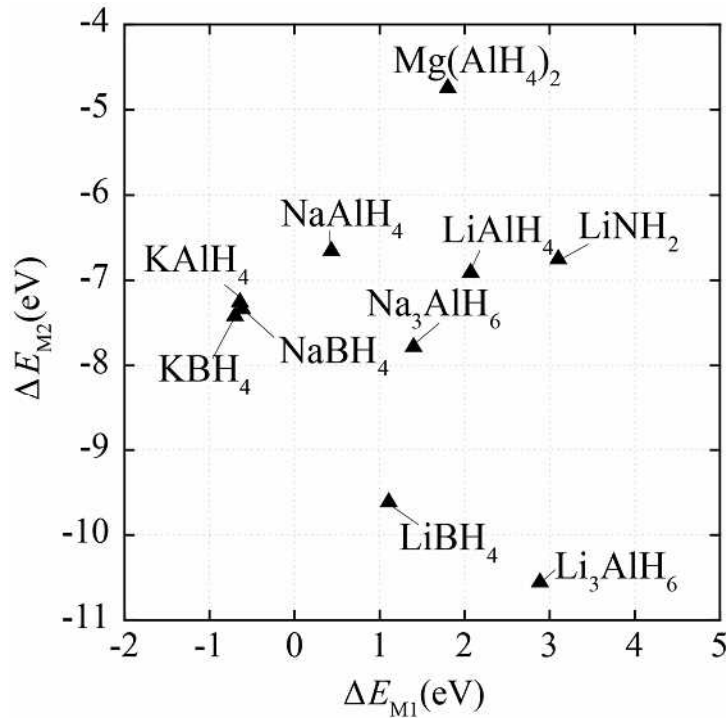


Fig. 3-14  $\Delta E_{M1}$  vs.  $\Delta E_{M2}$  diagram for complex hydrides.

### 3.3.6 Atomization energy diagram for hydrides and hydrocarbons

For a variety of crystalline hydrides such as binary hydrides, perovskite-type hydrides, metal hydrides, complex hydrides, and of hydrocarbons, an atomization energy diagram was constructed on an energy scale, as shown in Fig. 4-15. It is stressed here that every hydride can be shown in one figure, although there are significant differences in the nature of the chemical bonds among the hydrides, as described earlier.  $E_{coh}$ , given by Eq. (3), lies in the range 3–9 eV. As a whole, this range of  $E_{coh}$  ( $=\Delta E_H + \Delta E_M$ ) is much smaller compared with the ranges of atomization energy,  $0 \text{ eV} < \Delta E_H < 18 \text{ eV}$  and  $-11 \text{ eV} < \Delta E_M < 5 \text{ eV}$ . Thus, each atomic state is well controlled or balanced in the hydrides so as to make  $E_{coh}$  as large as possible. Among the hydrides, a binary hydride,  $AlH_3$ , shows the smallest cohesive energy, 3.2 eV, so it

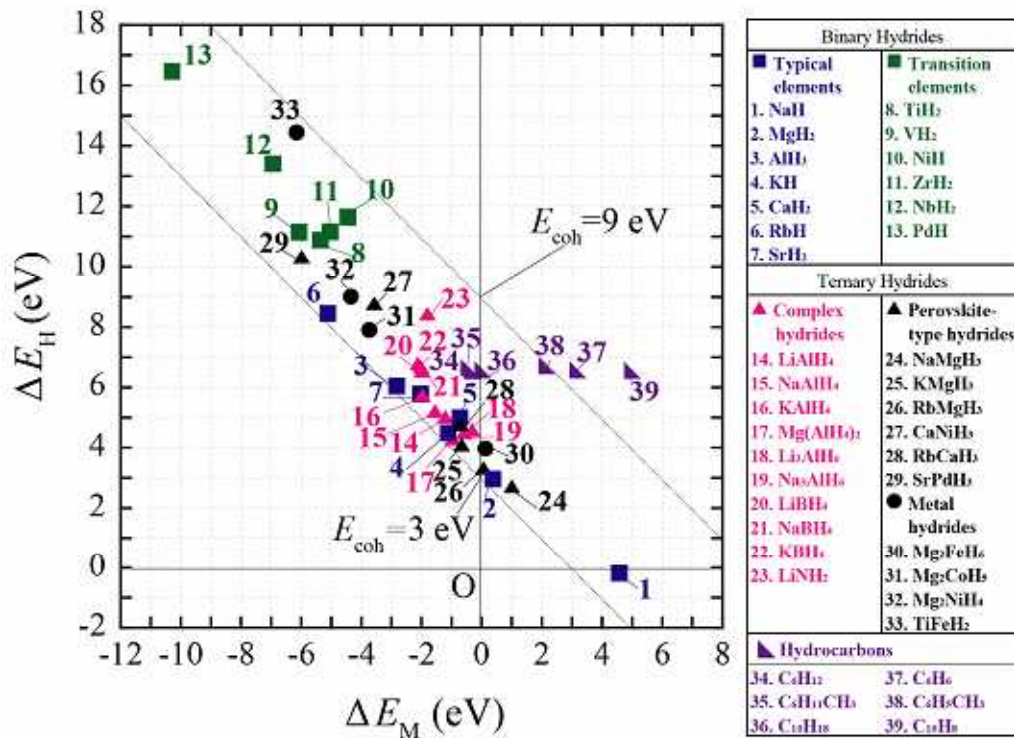


Fig. 3-15 Atomization energy diagram for crystalline hydrides and hydrocarbons.

releases hydrogen at a low temperature [37], but the re-hydrogenation reaction never occurs in the moderate condition because of its low stability. This is also seen in a complex hydride,  $\text{Mg}(\text{AlH}_4)_2$ , where both the  $E_{\text{coh}}$  and the  $\Delta E_{\text{H}}$  values are small.

It is evident from Fig. 3-15 that hydrides of transition elements have high  $\Delta E_{\text{H}}$  values. The region of complex hydrides is overlapped with that of the hydrides of the more common elements in this diagram. The locations of metal hydrides are distributed over the wide range of  $\Delta E_{\text{H}}$ , and some of them are located near the region of complex hydrides. In fact,  $\text{Mg}_2\text{NiH}_4$ ,  $\text{Mg}_2\text{CoH}_5$  and  $\text{Mg}_2\text{FeH}_6$  are sometimes treated as complex hydrides instead of metal hydrides [38]. In Fig. 3-15,  $\text{Mg}_2\text{FeH}_6$  and  $\text{Mg}_2\text{CoH}_5$  are located near the lower and upper region of complex hydrides, respectively. However,  $\text{Mg}_2\text{NiH}_4$  is located in the region between the hydrides of transition elements and the complex hydrides, indicating the coexistence of the characteristics of both metal and

complex hydrides in  $\text{Mg}_2\text{NiH}_4$ . Thus, the atomization energy diagram reflects important characteristics of the chemical bonds in hydrides.

### 3.4 Conclusion

An atomization energy diagram, which is obtained by EDA, is constructed to treat the chemical interactions in hydrides in an energy scale. All the crystalline hydrides, such as binary hydrides, perovskite-type hydrides, metal hydrides and complex hydrides, can be located on this diagram, although there are significant differences in the nature of the chemical bonds among the hydrides. Also, for hydrocarbon,  $\Delta E_C$  increases linearly with the ratio of the carbon number to the hydrogen number,  $m/n$ , while  $\Delta E_H$  remains constant. This indicates that the chemical stability of  $\text{C}_m\text{H}_n$  is dependent only on the  $m/n$  ratio.

Since the sum of the atomization energy equals the cohesive energy, each of the atomization energies is a measure of the chemical bonding effect of the element on the stability of the hydride. So, the roles of the constituent elements in crystalline hydrides and hydrocarbons can be understood well with the aid of this diagram.

The present unified approach based on the atomization energy concept is applicable to various crystalline materials and molecules. Therefore, it will provide us with a new tool for the quantitative comparison of chemical bonds in a variety of materials.

## REFERENCES

- [1] B. Bogdanovic and M. Schwickardi, *J. Alloys Comp.* 253-254 (1997) 1-9.
- [2] J. J. Reilly and R. H. Wiswall Jr, *Inorg. Chem.* 13 (1974) 218-222.
- [3] K. Komiya, N. Morisaku, R. Rong, Y. Takahashi, Y. Shinzato, H. Yukawa and M. Morinaga, *J. Alloys Comp.* in press. doi:10.1016/j.jallcom.2006.11.116
- [4] J. J. Reilly and R. H. Wiswall, Jr, *Inorg. Chem.* 7 (1968) 2254-2256.
- [5] L. Schlapbach, and A. Züttel, *Nature* 414 (2001) 353-358.
- [6] P. Chen, Z. Xiong, J. Luo, J. Lin, K. L. Tan, *Nature* 420 (2002) 302-304.
- [7] B. Bogdanovic, R. A. Brand, A. Marjanovic, M. Schwickardi and J. Tolle, *J. Alloys Comp.* 302 (2000) 36-58.
- [8] T. Ichikawa, S. Isobe, N. Hanada and H. Fujii, *J. Alloys Comp.* 365 (2004) 271-276.
- [9] Y. Nakamori, K. Miwa, A. Ninomiya, H. Li, N. Ohba, S. Towata, A. Züttel and S. Orimo, *Phys. Rev. B* 74 (2006) 045126(1)-045126(9).
- [10] S. V. Alapati, J. K. Johnson and D. S. Sholl, *Physical Chemistry Chemical Physics* 9 (2007) 1438-1452.
- [11] S. Hodoshima, H. Arai and Y. Saito, *Int. J. Hydrogen Energ.* 28 (2003) 197-204.
- [12] W. Kohn and L. J. Sham, *Phys. Rev.* 140 (1965) A1133-A1138.
- [13] J. P. Perdew, K. Burke and Y. Wang, *Phys. Rev. B* 41 (1970) 7892-7895.
- [14] V. Milman, B. Winkler, J. A. White, C. J. Pickard, M. C. Payne, E. V. Akhmatovskaya and R. H. Nudmann, *Int. J. Quant. Chem.* 77 (2000) 895-910.
- [15] D. Vanderbilt, *Phys. Rev. B* 41 (1990) 7892-7895.
- [16] M. Dewar, W. J. Thiel, *J. Am. Chem. Soc.* 99 (1977) 4899-4907.
- [17] J. C. Slater, *Phys. Rev.* 81 (1951) 385-390.
- [18] A. D. Becke, *Phys. Rev. A.* 38 (1988) 3098-3100.
- [19] S. H. Vosko, L. Wilk and M. Nusair, *Can. J. Phys.* 58 (1980) 1200-1211.
- [20] C. Lee, W. Yang and R. G. Parr, *Phys. Rev. B.* 37 (1988) 785-789.
- [21] T. H. Dunning, *J. Chem. Phys.* 90 (1989) 1007-1023.
- [22] D. E. Woon and T. H. Dunning, *J. Chem. Phys.* 98 (1993) 1358-1371.
- [23] A. Schafer, C. Huber and R. Ahlrichs, *J. Chem. Phys.* 100 (1994) 5829-5835.
- [24] S. Huzinaga, J. Andzelm, M. Klobukowski, E. Radzioandzelm, Y. Sakai, H. Tatewaki, *Gaussian Basis sets for Molecular Calculation*, Elsevier, New York, 1984.
- [25] V. A. Rassolov, J. A. Pople, M. Ratner and T. L. Windus, *J. Chem. Phys.* 109 (1998) 1223-1229.

- [26] W.J. Hehre, R. Ditchfield and J.A. Pople, *J. Chem. Phys.* 56 (1972) 2257-2261.
- [27] K.D.Dobbs and W.J. Hehre, *J. Comput. Chem.* 7 (1986) 359-378.
- [28] A. Schafer, H. Horn and R. Ahlrichs, *J. Chem. Phys.* 97 (1992) 2571-2577.
- [29] H. Nakai, Y.Kurabayashi, M.Katouda and T. Atsumi, *Chem. Phys. Lett.* 438 (2007) 132-138.
- [30] H. Nakai, *Chem. Phys. Lett.* 363 (2002) 73-79.
- [31] Y. Fukai, *The metal-hydrogen system*, Springer-Verlag, 1994.
- [32] R. C. Weast, M. J. Astle and W. H. Beyer, *CRC Handbook of Chemistry and Physics, A Ready-reference Book of Chemical and Physical Data (84th ed.)*, CRC Press, 2003.
- [33] M. Saeys, M. F. Reyniers, G. B. Marin, V. V. Spebroeck and M. Waroquier, *J. Phys. Chem. A* 107 (2003) 9147-9159.
- [34] G. C. Pimentel, R. D. Spratley, *Chemical bonding clarified through quantum chemistry*, Holden-day, Inc., 1969.
- [35] M. Yoshino, K. Komiya, Y. Takahashi, Y. Shinzato, H. Yukawa and M. Morinaga, *J. Alloys Comp.* 404-406 (2005) 185-190.
- [36] K. Komiya, N. Morisaku, Y. Shinzato, K. Ikeda, S. Orimo, Y. Ohki, K. Tatsumi, H. Yukawa and M. Morinaga, *J. Alloys Comp.* 446-447 (2007) 237-241.
- [37] J. Graetz, J. J. Reilly, *J. Alloys Comp.* 424 (2006) 262-265.
- [38] K. Yvon, *Chimia* 52 (1998) 613-619.

## Chapter 4 Analysis of the chemical bond in metal oxides based on the atomization energy concept

### 4.1 Introduction

The nature of the chemical bond in oxides would be related to the local structure such as the interionic distance and the coordination number. In any oxide structure, metal ions are surrounded by oxide ions to form polyhedra such as the octahedron and the tetrahedron. These polyhedra are linked together by sharing corner, edge or face as shown in Fig. 4-1. The sharing state is related to the composition and the density of oxides (i.e., average structure). Such a sharing effect together with the composition and the density would be related to the nature of the chemical bond. However, along the total energy calculation alone, the information of the chemical bond between ions in the local structure and average structure is still limited.

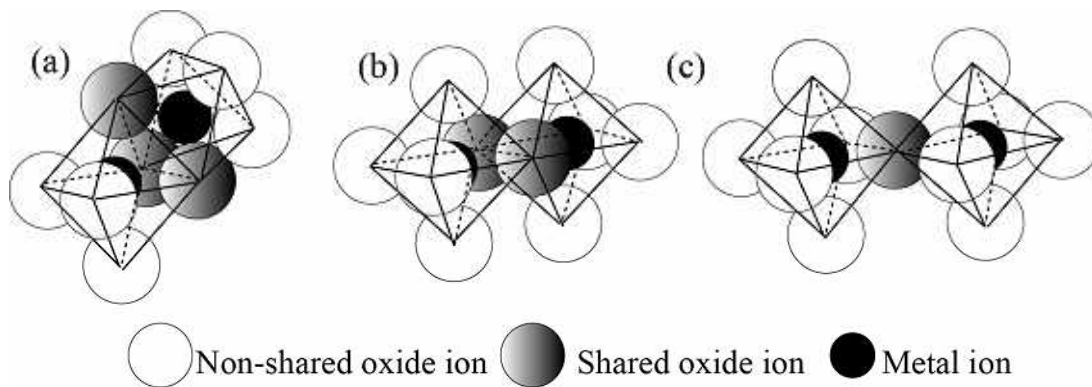


Fig. 4-1  $MO_6$  octahedra of (a) face, (b) edge and (c) corner sharing.

As mentioned in Chapter 1, metal oxides possess a wide variety of chemical and physical properties such as superconductivity, ferroelectricity, magnetism, catalyst and proton conductivity [1]. It is known that such properties (e.g., ferroelectricity) are related to the phase transition of oxides. For example, for perovskite-type oxides,

BaTiO<sub>3</sub>, phase transition occurs mainly the cooperative displacement of both Ti and O ions along the <100> direction as shown in Fig. 4-2 (a) [2]. As a result, BaTiO<sub>3</sub> undergoes a structural phase transition from cubic phase (paraelectric phase) to tetragonal phase (ferroelectric phase). On the other hand, for perovskite-type oxides such as CaTiO<sub>3</sub>, SrTiO<sub>3</sub>, CaZrO<sub>3</sub> and SrZrO<sub>3</sub>, phase transition occurs mainly by tilting of TiO<sub>6</sub> (or ZrO<sub>6</sub>) octahedra around O-Ti (or Zr)-O crystal axes as shown in Fig. 4-2 (b) [3, 4]. The structural stability has been treated following total energy calculation [5, 6, 7]. Also, the calculations of phonon mode [8, 9] and the Mulliken population analysis [10] have been performed to understand the phase transition of perovskite-type oxides.

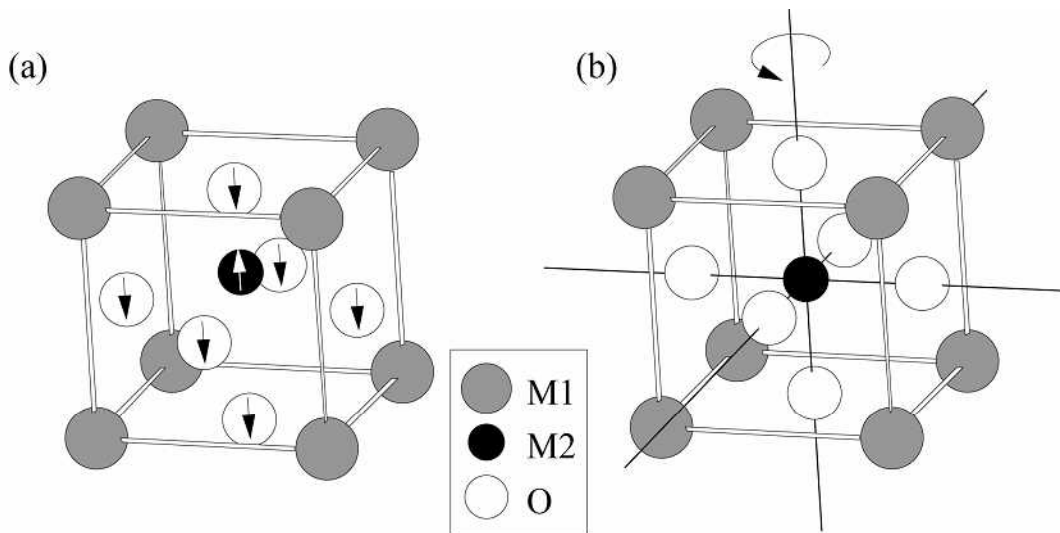


Fig. 4-2 Schematic illustration of (a) displacement-type and (b) tilting-type phase transitions [10].

Following the background, in this chapter, special attention is directed toward binary metal oxides such as zirconia (ZrO<sub>2</sub>), binary Cr, Ti and Fe oxides and perovskite-type oxides. Energy analyses of the chemical bond in these metal oxides are performed in view of the local structure, average structure and phase transition. Some ternary oxides such as sodium ferrites and spinel-type oxides, and binary metal carbides and nitrides are treated.

## 4.2 Calculation procedure

### 4.2.1 Geometry optimization and EDA calculation

The crystal structures of oxides are optimized by total energy minimization using the plane-wave pseudopotential method. For this purpose, first-principle calculations based on DFT [11] were performed with the generalized gradient approximation of Perdew et al [12]. The implementation of DFT employed here combines a plane-wave basis set with the total energy pseudopotential method, as embodied in the CASTEP code [13]. The present calculations were based upon the ultrasoft pseudopotentials proposed by Vanderbilt [14]. The plane-wave cutoff energy was chosen to be 380 eV. The sampling in the reciprocal space was done with  $k$ -point grids, e.g.,  $6 \times 6 \times 6$  for cubic  $\text{Na}_2\text{O}$  and  $8 \times 8 \times 8$  for cubic  $\text{CaTiO}_3$ .

The electronic structures for optimized crystal lattice of hydrides are obtained by the DFT calculations under the periodic boundary condition (PBC) using the Gaussian03 program package (Gaussian, Inc., Wallingford, CT). The adopted functional is the BLYP functional, which consists of the Slater exchange [15], the Becke (B88) exchange [16], the Vosko-Wilk-Nusair (VWN) correlation [17] and the Lee-Yang-Parr (LYP) correlation functionals [18]. The following modified Gaussian basis sets are adopted: (i) the Ahlrichs pVDZ [19] basis set without the outer  $s$  function and constructed to be double zeta class for Mg and Fe, (ii) the Ahlrichs TZV basis set [20] without the outer  $s$  function for K, (iii) the Huginaga basis sets [21] without the outer  $s$  function and constructed to be double zeta class for Na, V, Cr, Ni, Zr and Nb, (iv) the 6-31G basis sets [22, 23] without outer  $s$  function for O, Al, Ti and Ca and (v) the 3-21G basis set [24] without outer  $s$  function for Sr. In this study, the EDA calculations under PBC [25] are performed by linking the original code for the EDA with Gaussian03. Further

detailed explanation of the EDA calculation is given elsewhere [25, 26].

#### 4.2.2 Atomization energy

The EDA analysis is performed with the geometry optimized by the plane-wave pseudopotential method. For binary oxides, MO, the respective atomic energy densities of M and O are related closely to the nature of the chemical bond relevant to M and O atoms in MO. When the energy of the isolated neutral atom,  $E_M^{\text{atom}}$  (or  $E_O^{\text{atom}}$ ), is taken as a reference, the atomization energy,  $\Delta E_M$  (or  $\Delta E_O$ ) is defined as,

$$\Delta E_M = E_M^{\text{atom}} - E_M^{\text{oxide}}, \quad (1)$$

$$\Delta E_O = E_O^{\text{atom}} - E_O^{\text{oxide}}, \quad (2)$$

where  $E_M^{\text{oxide}}$  and  $E_O^{\text{oxide}}$  are the atomic energy densities for M and O in MO, respectively. Then, the cohesive energy,  $E_{\text{coh}}$ , of the oxide per oxygen atom is written as,

$$\Delta E_M + \Delta E_O = E_{\text{coh}}. \quad (3)$$

Thus,  $\Delta E_M$  and  $\Delta E_O$  are the components of  $E_{\text{coh}}$ .

In case of ternary oxides,  $(M1_xM2_y)O_z$ ,  $\Delta E_M$  is defined as  $(x\Delta E_{M1}+y\Delta E_{M2})/z$ , that is the average atomization energy of M1 and M2 to be counted per oxygen atom. Even in the other type of ternary oxides,  $\Delta E_M$  is defined in a similar way.

By setting that  $y = \Delta E_O$  and  $x = \Delta E_M$ , we obtain a relation,  $y = -x + E_{\text{coh}}$ . So,  $E_{\text{coh}}$  is expressed as a point of intersection of this line and y-axis at  $x = 0$ .

### 4.3 Results and discussion

#### 4.3.1 Cohesive energy for binary metal oxides

The cohesive energy,  $E_{\text{coh}}$ , is a measure of the electronic stability of oxides. As

shown Table 4-1, except for FeO, the difference between the calculated and the experimental values for  $E_{\text{coh}}$  lies within 0.47 eV [27]. Thus, the present calculations were performed in a reasonable manner.

Table 4-1 Calculated and experimental cohesive energies for binary metal oxides. (units: eV)

	$E_{\text{coh}}$ (Calc.)	$E_{\text{coh}}$ (Exp.)		$E_{\text{coh}}$ (Calc.)	$E_{\text{coh}}$ (Exp.)
Na <sub>2</sub> O	9.16	9.10	Cr <sub>2</sub> O <sub>3</sub>	9.19	9.26
MgO	9.91	10.34	CrO <sub>2</sub>	8.13	7.74
Al <sub>2</sub> O <sub>3</sub>	10.67	10.65	FeO	8.85	9.68
K <sub>2</sub> O	7.90	8.17	Fe <sub>3</sub> O <sub>4</sub>	8.41	8.69
CaO	11.08	11.01	Fe <sub>2</sub> O <sub>3</sub>	8.28	8.28
TiO <sub>2</sub>	10.23	9.93	SrO	10.27	10.41
TiO	12.83	12.88	Nb <sub>2</sub> O <sub>5</sub>	9.31	9.51
Ti <sub>2</sub> O <sub>3</sub>	11.44	11.11	ZrO <sub>2</sub>	11.13	11.40
V <sub>2</sub> O <sub>3</sub>	10.60	10.35	MoO <sub>2</sub>	9.12	9.05
			BaO	10.50	10.18

### 4.3.2 Binary metal oxides

#### (1) Local structure and average structure

##### (a) Interionic distance and coordination number

The nature of the chemical bond in metal oxides is related to the local structure such as the M-O distance and the coordination number. Thus, for binary metal oxides, the correlation is investigated between the local structure such as M-O interionic distances,  $d_{\text{M-O}}$ , and the coordination number,  $CN$ , and the atomization energy. For example, the  $\Delta E_{\text{O}}$  vs.  $\Delta E_{\text{M}}$  diagram (i.e., atomization energy diagram) for binary Cr oxides is shown in Fig. 4-3. There is a clear trend that  $\Delta E_{\text{O}}$  increases with decreasing  $\Delta E_{\text{M}}$ .  $\Delta E_{\text{O}}$  changes in the order,  $\text{CrO}_3 > \text{CrO}_2 > \text{Cr}_2\text{O}_3 > \text{CrO}$ . This is the reverse order of the average Cr-O neighbor distance,  $d_{\text{Cr-O}}$ ,  $\text{CrO}_3 < \text{CrO}_2 < \text{Cr}_2\text{O}_3 < \text{CrO}$  as shown in Table 4-2. This

Table 4-2 Atomic arrangements in binary Cr oxides.

	CrO <sub>3</sub>	CrO <sub>2</sub>	Cr <sub>2</sub> O <sub>3</sub>	CrO
$d_{\text{Cr-O}}$ (nm)	0.166	0.188	0.195	0.206
CN(Cr)	4	6	6	6
CN(O)	1,2	3	4	6

indicates that oxygen state in binary Cr oxides is stabilized owing to the shorter Cr-O interionic distance. In addition, the coordination number of O around Cr,  $CN(\text{Cr})$ , changes in this order,  $\text{CrO}_3 < \text{CrO}_2 = \text{Cr}_2\text{O}_3 = \text{CrO}$  as shown in Table 4-2. Thus, the oxide state is more stable in  $\text{CrO}_3$  than in  $\text{CrO}_2$ ,  $\text{Cr}_2\text{O}_3$  and  $\text{CrO}$  as might be expected from the coordination number effect. In addition,  $\Delta E_{\text{O}}$  is the highest, although  $\text{CrO}_3$  has the lowest cohesive energy among the binary Cr oxides.

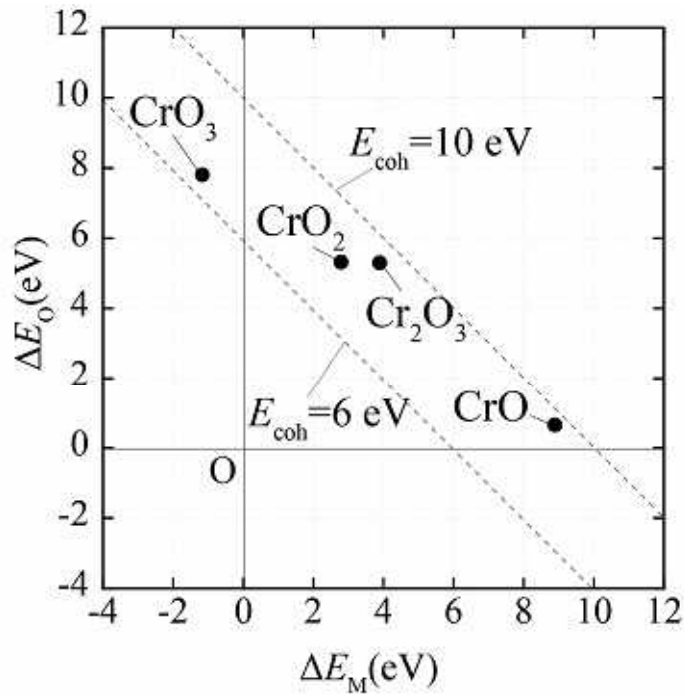


Fig. 4-3 Atomization energy diagram for binary Cr oxides.

(b) Linkage of polyhedra

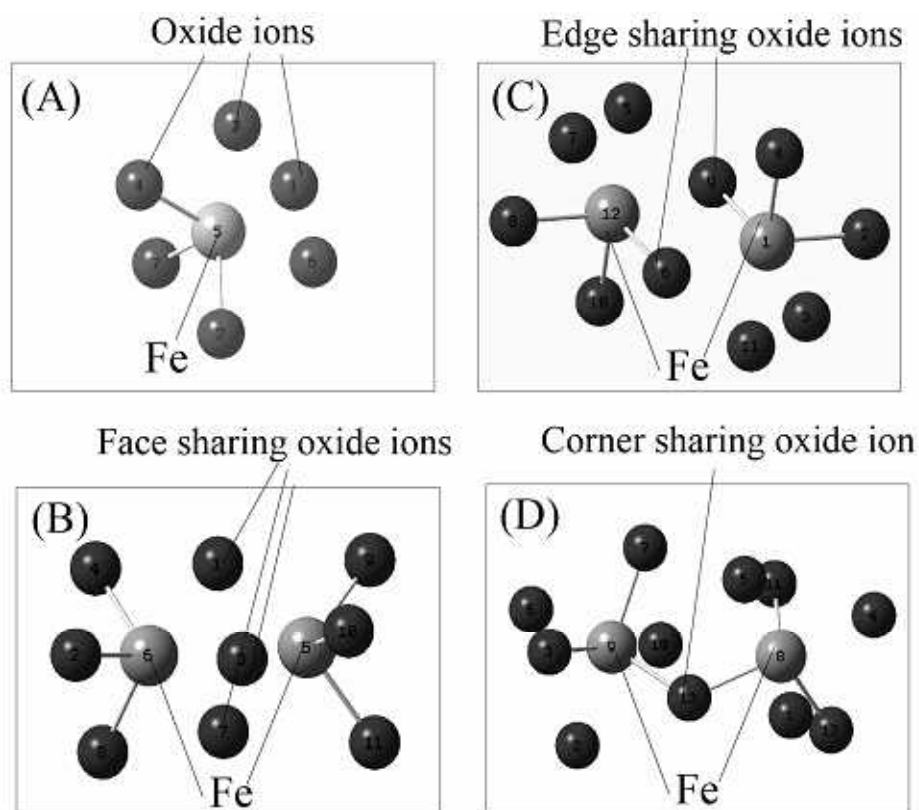


Fig. 4-4 Calculated  $\text{Fe}_2\text{O}_3$  clusters of (A) one octahedron, and three clusters of octahedra shared by (B) face, (C) edge and (D) corner.

In any oxide structures, polyhedra such as octahedron and tetrahedron are present, and they are linked together by corner, edge or face sharing. In this section, to investigate this linkage effect of polyhedra on the chemical bond, the calculations of four clusters were carried out. The cluster models were constructed on the basis of the crystal structure of  $\text{Fe}_2\text{O}_3$ , as shown in Fig. 4-4. The calculated atomization energies for Fe,  $\Delta E_{\text{Fe}}$ , in cluster (A)-(D) are 0.1, -1.7, -1.7 and 1.2 eV, respectively. The Fe-Fe distances are 0.259, 0.275 and 0.332 nm in cluster (B), (C) and (D) respectively. The long Fe-Fe distance tends to weaken the repulsive Coulomb interaction between them. The atomization energies for oxide ion (or shared oxide ion),  $\Delta E_{\text{O}}$ , in cluster (A)-(D) are

3.5, 5.9, 6.7 and 6.2 eV, respectively. It is evident that the oxide ion state is stabilized by sharing. The oxide ion in the edge shared cluster is most stable among the three shared clusters. This is probably a reason why polyhedra are linked edge sharing in many oxides. This trend is also seen in the sodium ferrites such as  $\text{Na}_2\text{FeO}_4$ ,  $\text{Na}_4\text{FeO}_4$ ,  $\text{NaFeO}_2$ ,  $\text{NaFe}_2\text{O}_3$  and  $\text{Na}_4\text{FeO}_3$ . These sodium ferrites change the formal charge state of the Fe ion as follows,  $\text{Na}_2\text{FeO}_4$  (+6),  $\text{Na}_4\text{FeO}_4$  (+4),  $\text{NaFeO}_2$  (+3),  $\text{NaFe}_2\text{O}_3$  (+2.5) and  $\text{Na}_4\text{FeO}_3$  (+2). In  $\text{NaFeO}_2$  and  $\text{NaFe}_2\text{O}_3$ , the edge sharing is dominant, whereas in  $\text{Na}_2\text{FeO}_4$ ,  $\text{Na}_4\text{FeO}_3$  and  $\text{Na}_4\text{FeO}_4$ , there is no sharing. As shown in Fig. 4-5, the oxide ion is more stabilized in  $\text{NaFeO}_2$  and  $\text{NaFe}_2\text{O}_3$  than in  $\text{Na}_2\text{FeO}_4$ ,  $\text{Na}_4\text{FeO}_3$  and  $\text{Na}_4\text{FeO}_4$ . This trend may be interpreted as due to the sharing effect.

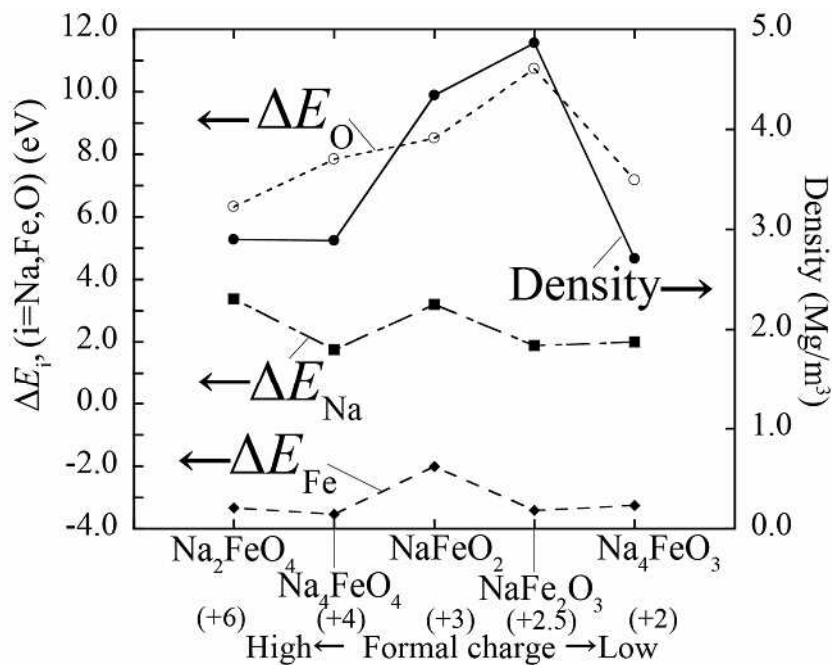


Fig. 4-5 Atomization energy for constituent elements in sodium ferrites.

(c) Density

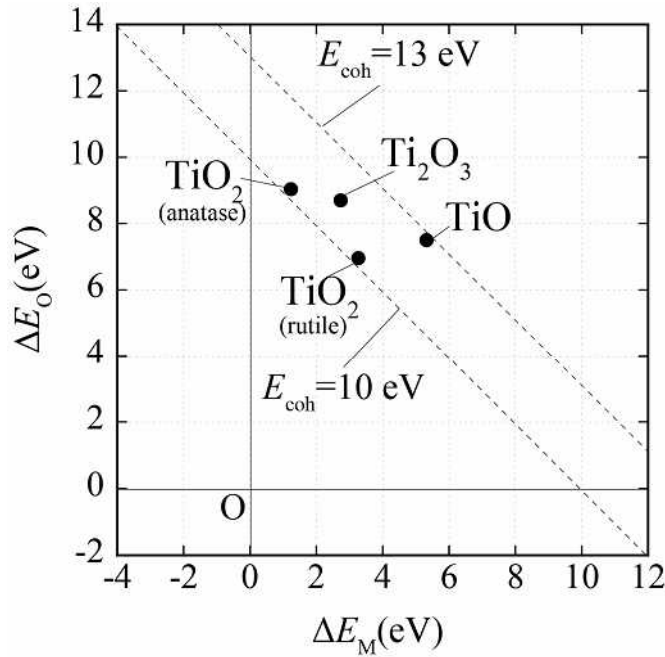


Fig. 4-6 Atomization energy diagram for binary Ti oxides.

Atomization energy diagram for binary Ti oxides is shown in Fig. 4-6. For  $\text{TiO}_2$ ,  $\Delta E_O$  is larger in anatase than in rutile, although the local ionic arrangements are almost similar between them as shown in Table 4-3. This may be due to the difference in the density between anatase ( $3.84 \text{ Mg/m}^3$ ) and rutile ( $4.24 \text{ Mg/m}^3$ ). A correlation between the atomization energy and the density in binary oxides are shown in Fig. 4-7. There is a clear trend that  $\Delta E_M$  increases and  $\Delta E_O$  decreases with increasing density of oxides. This is seen clearly in the zirconia shown in Fig. 4-7 (d). As a compositional ratio of M/O increases, the metal state is stabilized, but the oxide ion state is destabilized in

Table 4-3 Atomic arrangements in binary Ti oxides.

	$\text{TiO}_2$ (anatase)	$\text{TiO}_2$ (rutile)	$\text{Ti}_2\text{O}_3$	$\text{TiO}$
$d_{\text{Ti-O}}$ (nm)	0.196	0.197	0.204	0.214
CN(Ti)	6	6	6	6
CN(O)	3	3	4	6

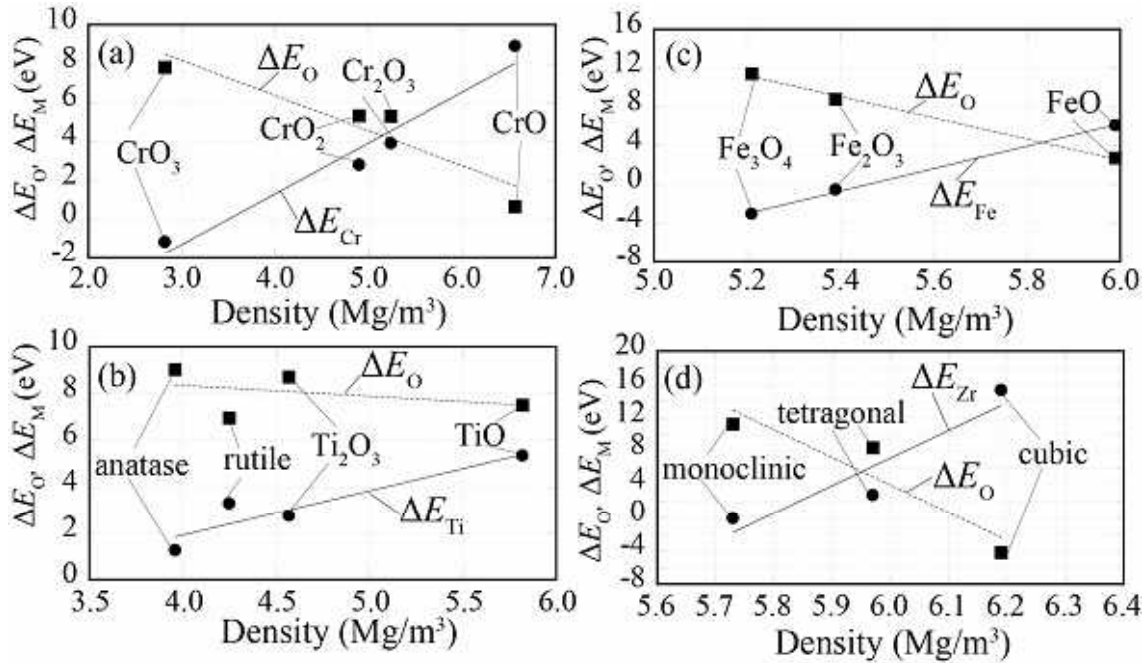


Fig. 4-7 Correlation between atomization energy and density of (a) binary Cr oxides, (b) binary Ti oxides, (c) binary Fe oxides and (d) zirconia ( $ZrO_2$ ).

these binary oxides.

In case of sodium ferrites,  $\Delta E_O$  changes in the order,  $Na_2FeO_4 < Na_4FeO_3 < Na_4FeO_4 < NaFeO_2 < NaFe_2O_3$ , as shown in Fig. 4-5. This order approximately coincides with the order of density as shown in Fig. 4-5. Thus, the oxide ion state is stabilized with increasing density of oxides. However, this is the reverse of the results shown in Fig. 4-7. In Fig. 4-5,  $\Delta E_{Na}$  changes with the oxides in conjunction with  $\Delta E_{Fe}$ . This indicates that not only the Fe-O interaction but also the Na-Fe and the Na-O interactions are significant in them. Thus, the ternary oxides (sodium ferrites) behave in a somewhat different way from the binary oxides shown in Fig. 4-7, due to the effect of ternary element on the chemical bond in them.

(2) Charge states of metal ions

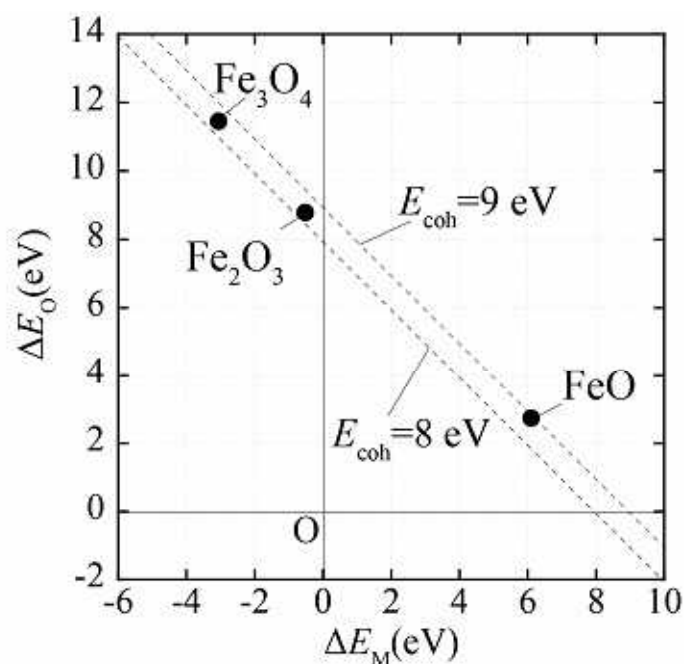


Fig. 4-8 Atomization energy diagram for binary Fe oxides.

There are three well known polymorphs;  $\text{FeO}$ ,  $\text{Fe}_2\text{O}_3$  and  $\text{Fe}_3\text{O}_4$ . Atomization energy for binary Fe oxides is shown in Fig. 4-10. Among binary Fe oxides, the atomization energy for oxygen,  $\Delta E_O$ , is positive and changes in the order,  $\text{Fe}_3\text{O}_4 > \text{Fe}_2\text{O}_3 > \text{FeO}$ . According to the Mulliken population analysis, the net charge on the O atom in them changes in the order,  $\text{Fe}_2\text{O}_3$  (-0.61)  $>$   $\text{Fe}_3\text{O}_4$  (-0.65)  $>$   $\text{FeO}$  (-0.72). This means that charge transfer occurs from metal ions to oxygen ions in them. Thus, the oxygen state in metal oxides is stabilized to some extent by the charge transfer. However, such a traditional analysis alone never explains a whole feature of the atomization energy diagram expressed in an energy scale.

Also, for sodium ferrites such as  $\text{Na}_2\text{FeO}_4$ ,  $\text{Na}_4\text{FeO}_4$ ,  $\text{NaFeO}_2$ ,  $\text{NaFe}_2\text{O}_3$  and  $\text{Na}_4\text{FeO}_3$ , there is no correlation between the formal charge states of Fe and  $\Delta E_{\text{Fe}}$  as shown in Fig. 4-5. Thus, along the concept of formal charge alone, it is difficult to understand the

chemical bond in oxides.

(3) Phase transition of  $ZrO_2$

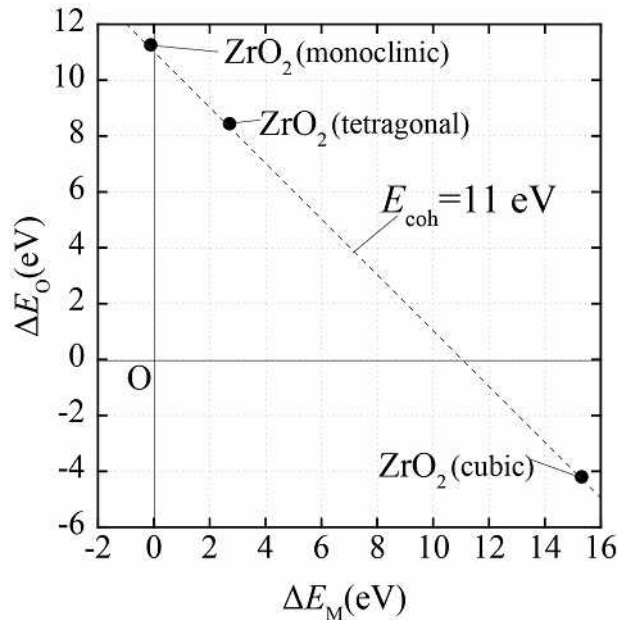


Fig. 4-9 Atomization energy diagram for zirconia,  $ZrO_2$ .

For zirconium dioxides,  $ZrO_2$  (zirconia), there are three well-known polymorphs; monoclinic, tetragonal and cubic phases. The monoclinic phase, which is stable below 1300 K, can be described as a distortion of the cubic  $CaF_2$  structure. At higher temperatures the tetragonal phase is stable, and it transform to the cubic phase at about 2600 K. The tetragonal phase of  $ZrO_2$  can be described as resulting from the displacement of oxide ions from cubic fluorite positions along  $\langle 100 \rangle$  directions. To investigate the change of the chemical bond by the phase transition, atomization energy diagram for  $ZrO_2$  is shown in Fig. 4-11.  $\Delta E_O$  changes in the order,  $ZrO_2$  (monoclinic) >  $ZrO_2$  (tetragonal) >  $ZrO_2$  (cubic). As shown in Table 4-4, the Zr-O average distance,  $d_{Zr-O}$ , and the coordination number,  $CN$ , are similar between  $ZrO_2$  (tetragonal) and  $ZrO_2$  (cubic). However, the  $\Delta E_O$  is higher in  $ZrO_2$  (tetragonal) than in  $ZrO_2$  (cubic). This may

Table 4-4 Atomic arrangements in zirconia ( $ZrO_2$ ).

	Monoclinic	Cubic	Tetragonal
$d_{Zr-O}$ (nm)	0.184	0.221	0.225
CN(Zr)	7	8	8
CN(O)	3	4	4

be interpreted as due to the repulsive Coulomb interaction between O-O ions. The average distance between oxide ions is 0.263 nm in  $ZrO_2$  (tetragonal) and 0.255 nm in  $ZrO_2$  (cubic). Thus, by the phase transition from cubic to tetragonal phase, the  $\Delta E_O$  is stabilized with decreasing repulsive energy between oxide ions. In other words, the density is lower in the tetragonal phase than in the cubic phase, resulting in the  $\Delta E_O$  change with the phase transition as shown in Fig. 4-9.

### 4.3.3 Perovskite-type oxides

(a) Energy balance among constituent elements and their contribution to cohesive energy

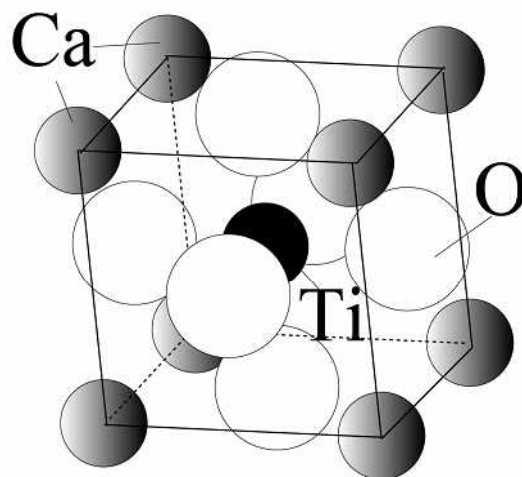


Fig. 4-10 Crystal structure of perovskite-type oxide,  $CaTiO_3$

The crystal structure of the perovskite-type oxides,  $CaTiO_3$ , is shown in Fig. 4-10.

Ca is located at the corner, Ti is located at the center, and O is located at the face center. As a result, Ti is surrounded by six oxide ions to form an octahedron.

The atomization energy diagram for perovskite-type oxides,  $M1M2O_3$  is shown in Fig. 4-11 together with some results of binary metal oxides for comparison. For every perovskite-type oxide indicated by open circles in Fig. 4-11,  $\Delta E_O$  is larger than  $\Delta E_M$ , indicating that the oxide ions contribute to the cohesive energy more significantly than metal ions. The cohesive energy,  $E_{coh}$ , of the perovskite-type oxides lies in the range 9-12 eV.

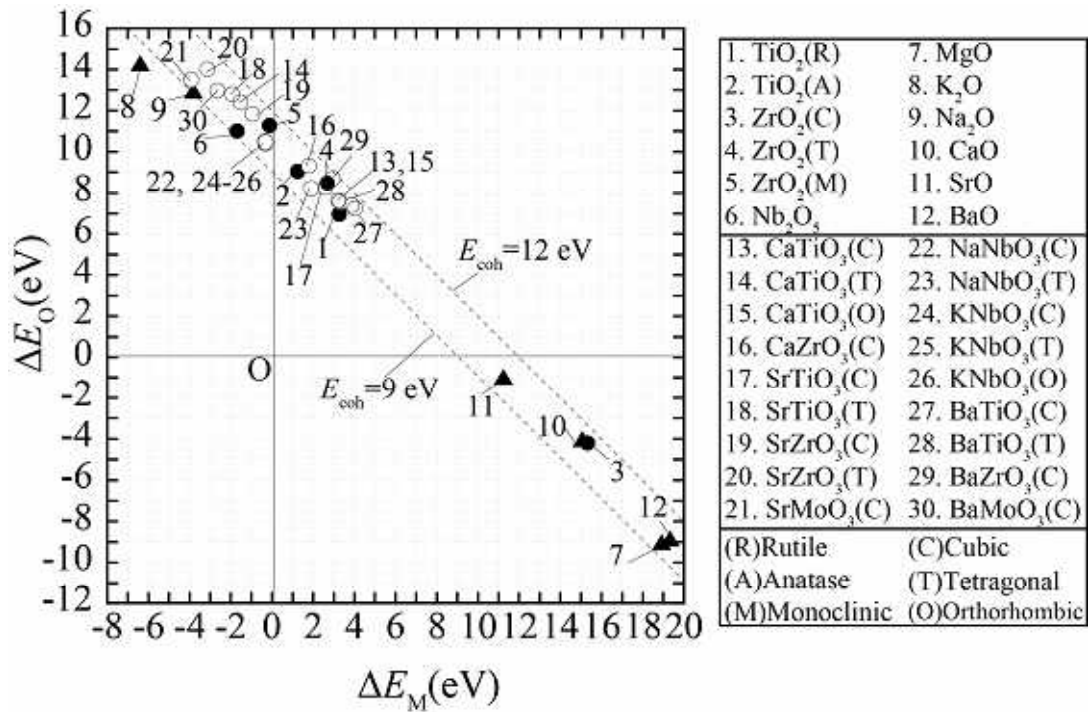


Fig. 4-11 Atomization energy diagram for perovskite-type oxides.

When the oxides have a resemblance in the chemical bonding state, their locations are close to each other in the diagram. In Fig. 4-11, perovskite-type oxide,  $M1M2O_3$  ( $= M1O + M2O_2$  or  $M1_2O + M2_2O_5$ ) is located near the binary oxides,  $M2O_2$  (or  $M2_2O_5$ ) in this diagram. For example, CaTiO<sub>3</sub> (No. 13, 14 or 15) is located closer to TiO<sub>2</sub> (rutile

(No. 1) and anatase (No. 2)) than CaO (No. 10). NaNbO<sub>3</sub> (No. 22 or 23) is located closer to Nb<sub>2</sub>O<sub>5</sub> (No. 6) than Na<sub>2</sub>O (No. 9). This indicates that the perovskite-type oxide inherits the nature of the chemical bond mainly from M<sub>2</sub>O<sub>2</sub> (or M<sub>2</sub>O<sub>5</sub>). For CaTiO<sub>3</sub>, average Ti-O distance changes in the order, CaTiO<sub>3</sub> (orthorhombic, 0.1970 nm) > CaTiO<sub>3</sub> (tetragonal, 0.1949 nm) > CaTiO<sub>3</sub> (cubic, 0.1935 nm). As shown in Fig. 4-11, this order is not in agreement with the order of  $\Delta E_O$  in CaTiO<sub>3</sub>, CaTiO<sub>3</sub>(T) > CaTiO<sub>3</sub>(C) = CaTiO<sub>3</sub>(O). This trend is seen in the other perovskite-type oxides. Thus, the oxide ion state is not interpreted by the average interionic distance. Also, in perovskite-type oxides, M<sub>1</sub>M<sub>2</sub>O<sub>3</sub>, M<sub>2</sub>O<sub>6</sub> octahedra are linked together by the corner sharing. However, the difference is not seen in oxide ion state between perovskite-type oxides and binary oxides, M<sub>2</sub>O<sub>2</sub> or M<sub>2</sub>O<sub>5</sub>. For example, TiO<sub>6</sub> octahedra in CaTiO<sub>3</sub> are linked together by the corner sharing. On the other hand, TiO<sub>6</sub> octahedra in TiO<sub>2</sub> (anatase) and TiO<sub>2</sub> (rutile) are linked together by the edge sharing. According to the sharing effect, it is expected that oxide state is more stabilized in TiO<sub>2</sub> than in CaTiO<sub>3</sub>. However, as shown in Fig. 4-11,  $\Delta E_O$  changes in the order, CaTiO<sub>3</sub>(T) > TiO<sub>2</sub>(A) > CaTiO<sub>3</sub>(C) = CaTiO<sub>3</sub>(O) > TiO<sub>2</sub>(R). Thus, oxide ion state is not interpreted by using the average interionic distance and sharing effect. These probably arise from the energy balance between M<sub>1</sub> and M<sub>2</sub> ions in perovskite-type oxides as described later. Not only M<sub>2</sub> ion but also M<sub>1</sub> ion plays an important role in the nature of the chemical bond between them.

As shown in Fig. 4-12, a  $\Delta E_{M1}$  vs.  $\Delta E_{M2}$  diagram is made to understand the role of metal elements in the formation of the chemical bond in the perovskite-type oxides, M<sub>1</sub>M<sub>2</sub>O<sub>3</sub>. The positions of SrM<sub>2</sub>O<sub>3</sub> (M<sub>1</sub> = Sr) except for SrMoO<sub>3</sub> (No. 21) are aligned along a line shown in the figure, indicating that there is a certain balance between

$\Delta E_{Sr}$  and  $\Delta E_{M2}$ . This trend is also seen in the cases of Ca, Ba and Na for M1. However, such a balance is no longer present in  $SrMoO_3$  as described above. This indicates that the Mo-O interaction is stronger in  $SrMoO_3$  (No. 21) than in  $BaMoO_3$  (No. 30) owing to shorter Mo-O distance. For example, any other  $SrM_2O_3$  oxides, resulting in the very large  $\Delta E_O$  (see Fig. 4-11, No.21) but the very small  $\Delta E_M$ . In particular,  $\Delta E_{M0}$  is smaller than  $\Delta E_{Sr}$ . The energy balance between  $\Delta E_{M0}$  and  $\Delta E_{Sr}$  is somewhat broken in  $SrMoO_3$ . The strong Mo-O interaction may be attributed to the shorter Mo-O distance. For example, average Mo-O distance is 0.1996 nm for  $SrMoO_3$ , 0.2037 nm for  $BaMoO_3$  and 0.2018 nm for  $MoO_2$ . As a result,  $\Delta E_O$  is very large and the balance is somewhat broken in  $SrMoO_3$ .

In addition, in perovskite-type oxides,  $\Delta E_{M1}$  and  $\Delta E_{M2}$  are very different, depending

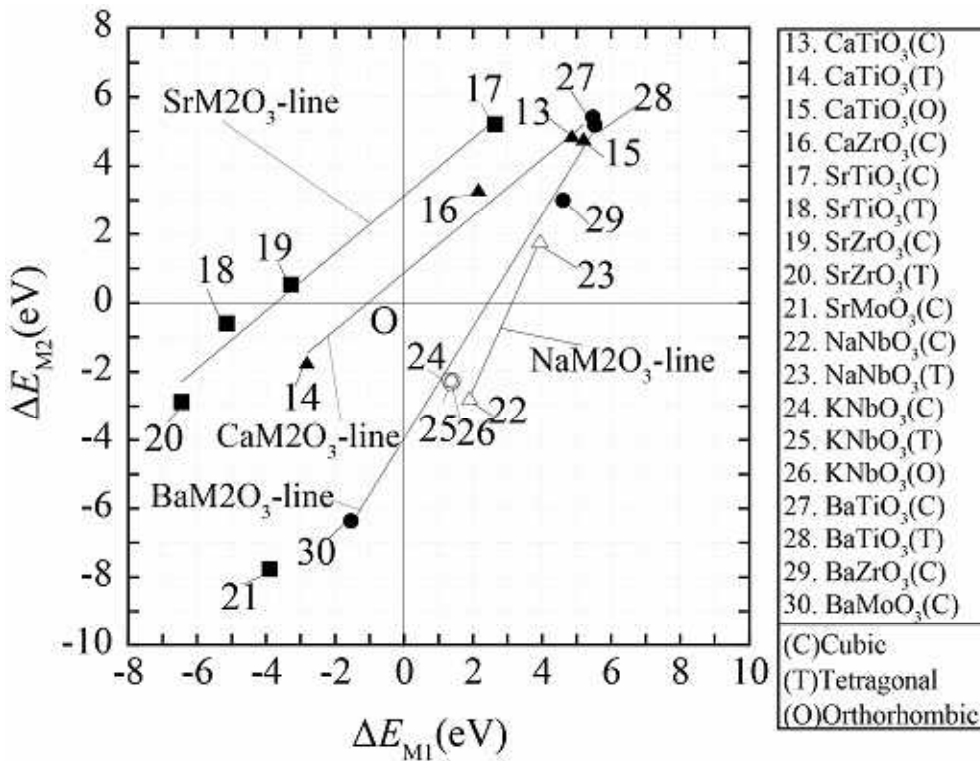


Fig. 4-12  $\Delta E_{M1}$  vs.  $\Delta E_{M2}$  diagram for perovskite-type oxides.

on the crystal structures. For example, the locations of  $\text{CaTiO}_3$  are dependent on the crystal structure (No. 13 for cubic structure and No. 14 for tetragonal structure).

(b) Comparison with spinel-type oxides

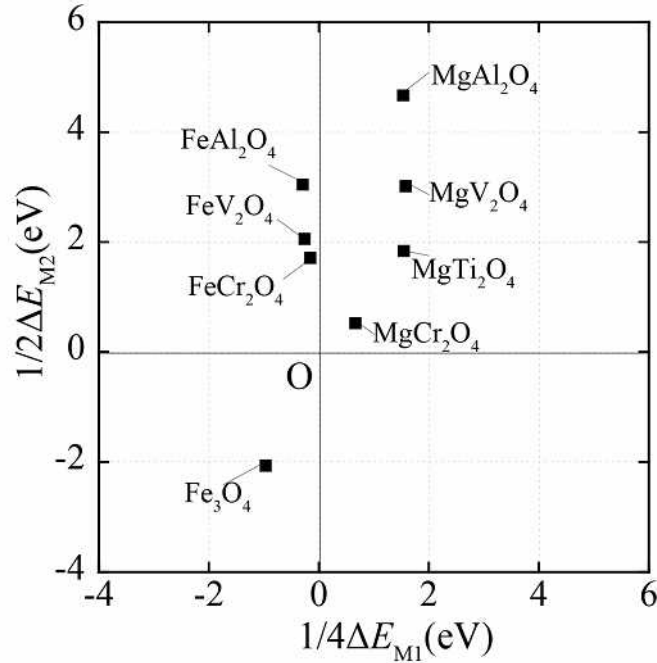


Fig.4-13  $\Delta E_{M1}$  vs.  $\Delta E_{M2}$  diagram for spinel-type oxides.

For comparison, a  $\Delta E_{M1}$  vs.  $\Delta E_{M2}$  diagram for spinel-type oxides,  $\text{M1M}_2\text{O}_4$ , is shown in Fig. 4-13. As shown in Fig. 4-13, for  $\text{FeM}_2\text{O}_4$  system ( $M_2 = \text{Fe, Cr, V, Al}$ ),  $\Delta E_{\text{Fe}}$  is nearly constant and  $\Delta E_{M_2}$  changes in the order,  $\text{Fe}_3\text{O}_4 < \text{FeCr}_2\text{O}_4 < \text{FeV}_2\text{O}_4 < \text{FeAl}_2\text{O}_4$ . This order is in agreement with the order of the atomization energy for  $M_2$  in binary oxides,  $\text{Fe}_2\text{O}_3 < \text{Cr}_2\text{O}_3 < \text{V}_2\text{O}_3 < \text{Al}_2\text{O}_3$ , as shown in Fig. 4-14. This trend is also seen in the  $\text{MgM}_2\text{O}_4$  system. Thus,  $M_2$  atomic state in the spinel-type oxides,  $\text{M1M}_2\text{O}_4$  ( $= \text{M1O} + \text{M}_2\text{O}_3$ ) inherits the nature of the chemical bond mainly from  $\text{M}_2\text{O}_3$ . This result is supported further by a strong correlation of the cohesive energy between the spinel-type oxides,  $\text{M1M}_2\text{O}_4$  and  $\text{M}_2\text{O}_3$  as shown in Fig. 4-15. This

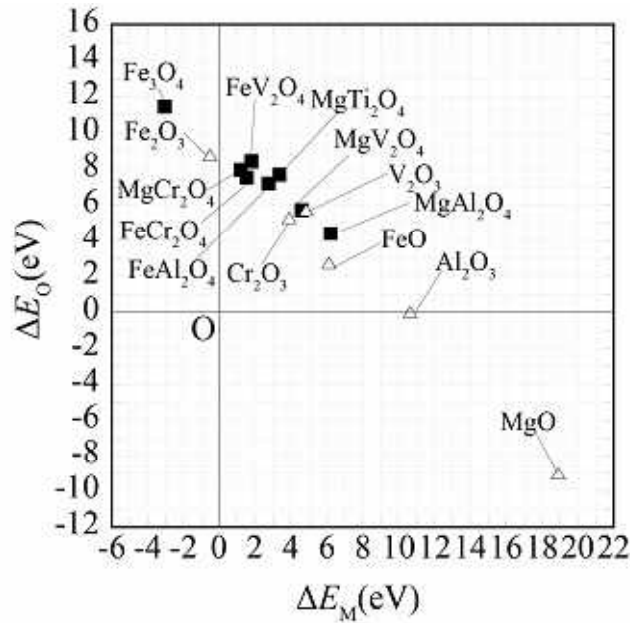


Fig. 4-14 Atomization energy diagram for spinell-type oxides and corundum oxides.

indicates that M2 elements play a significant role in the phase stability of  $\text{M1M}_2\text{O}_4$ . In this sense, an energy balance between M1 and M2 is not present in the spinell-type oxides.

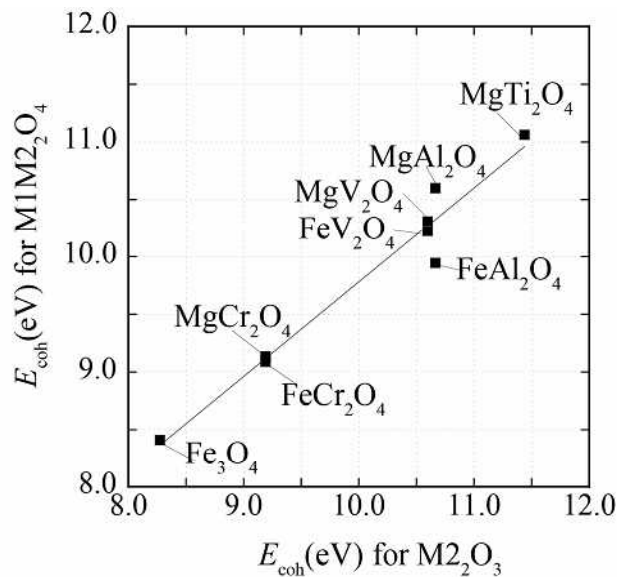


Fig. 4-15 Correlation of the cohesive energy between spinell-type oxides,  $\text{M1M}_2\text{O}_4$  and corundum oxides,  $\text{M}_2\text{O}_3$ .

In addition, it is noted that  $\Delta E_O$  is larger in  $\text{M1M}_2\text{O}_4$  than in  $\text{M}_2\text{O}_3$ . This may be

interpreted by the sharing effect. In both the spinel-type oxides,  $M_1M_2O_4$ , and corundum oxides,  $M_2O_3$ , M2 is surrounded by six oxide ions to form a  $M_2O_6$  octahedron. Such  $M_2O_6$  octahedra are linked together by the edge and corner sharing in spinel-type oxides,  $M_1M_2O_4$ , but by the face, edge and corner sharing in corundum oxides,  $M_2O_3$ . So, the oxide ion state in the corundum oxides is more destabilized compared to that in the spinel-type oxides owing to the presence of the unstable face shared oxide ions in  $M_2O_3$ .

#### (c) Phase transition of perovskite-type oxides

In this section, the analysis of chemical bond in perovskite-type oxides is performed to investigate these two type phase transition in view of the atomization energy. The calculated models of  $CaTiO_3$  used in this calculations are the crystal structures at room temperature, 1273, 1473, 1523 and 1633 K [28, 29]. In case of  $BaTiO_3$ , used are the crystal structures at room temperature, 1387 and 1645 K [30, 31]. The change of the atomization energy as a function of density in  $CaTiO_3$  and  $BaTiO_3$  is shown in Fig. 4-16. Here, the density is used instead of the temperature to show the  $\Delta E_i$  change with temperatures. The density decreases with increasing temperature. For  $CaTiO_3$ , the atomization energy varies significantly by tilting-type phase transition from cubic to tetragonal phase. On the other hand, the change of the atomization energy with the density is relatively small. The atomization energy change with the phase transition is much lower in  $BaTiO_3$  than in  $CaTiO_3$ . However, in either oxide,  $\Delta E_O$  increases by the phase transition from cubic phase to tetragonal phase. This trend is seen in other perovskite-type oxides.

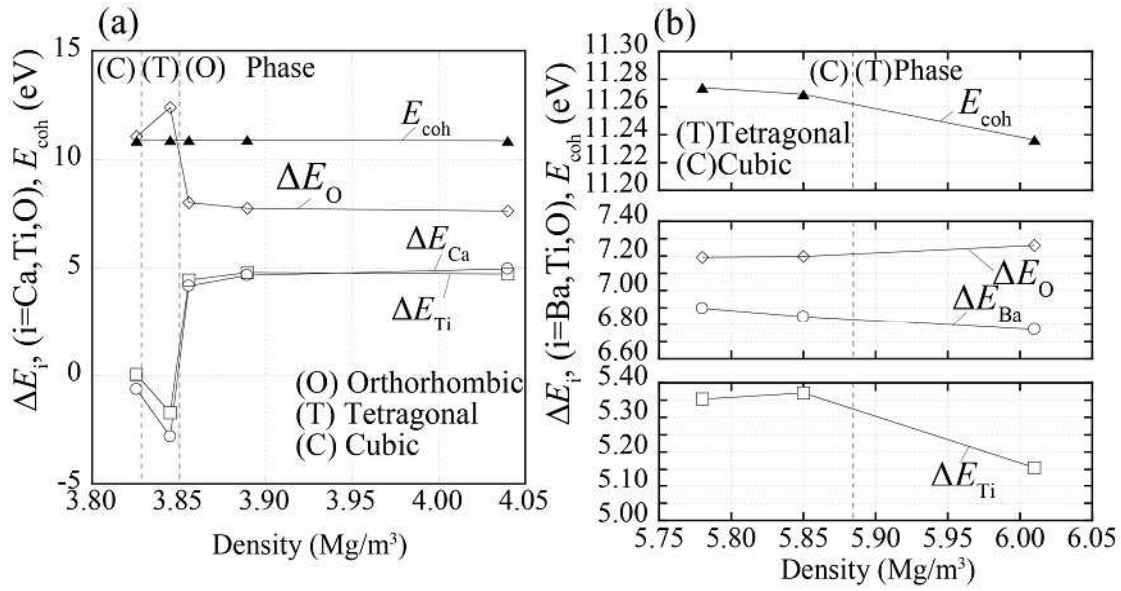


Fig. 4-16 Change of the atomization energy as a function of density for (a)  $\text{CaTiO}_3$  and (b)  $\text{BaTiO}_3$ .

As another sample, in Fig. 4-17, the change of the atomization energy is shown as a function of the density of  $\text{SrTiO}_3$  and  $\text{SrZrO}_3$ . The phase transition from cubic phase to tetragonal phase makes the oxide ion state stable in  $\text{SrTiO}_3$  and  $\text{SrZrO}_3$ . This is similar to the result shown in Fig. 4-16.

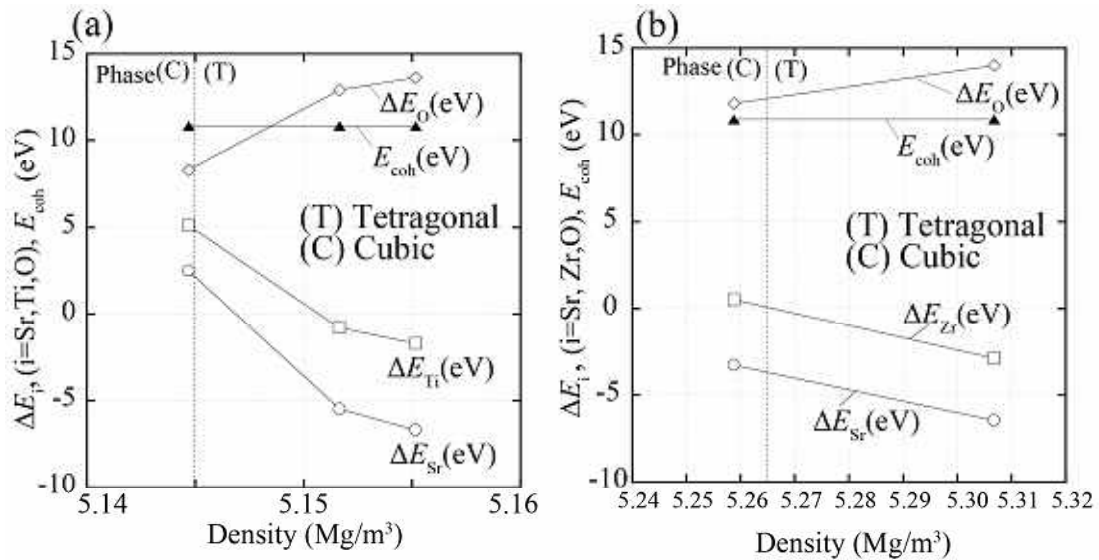


Fig. 4-17 Change of the atomization energy as a function of density for (a)  $\text{SrTiO}_3$  and (b)  $\text{SrZrO}_3$ .

In  $\text{CaTiO}_3$ , the average O-O distance increases by tilting of  $\text{TiO}_6$  octahedra. The

longer O-O distance tends to weaken the O-O repulsive Coulomb interaction, resulting in a large gain of  $\Delta E_O$  by tilting. On the other hand, it is supposed that the average O-O distance in  $\text{BaTiO}_3$  is scarcely changed by the phase transition from cubic to tetragonal phase. This is because, all the O ions are displaced in the same way along a  $\langle 100 \rangle$  direction by the phase transition from cubic to tetragonal phase. As a result, the change of  $\Delta E_O$  is very limited. This trend is also seen in  $\text{KNbO}_3$ .

As shown in Fig. 4-12, both  $\Delta E_{M1}$  and  $\Delta E_{M2}$  in  $\text{NaNbO}_3$  (No. 22, 23) increase by phase transition from cubic to tetragonal phase. This is reverse trend of  $\text{CaTiO}_3$  (No. 13, 14). This is probably due to rotate direction. Fig 4-18 shows a view looking down the  $z$  axis of octahedral for  $\text{CaTiO}_3$  and  $\text{NaNbO}_3$ . As shown Fig. 4-18 (a), in case of  $\text{CaTiO}_3$ , rotation of one  $\text{TiO}_6$  octahedron forces four of the neighboring six octahedra to rotate in the opposite sense. Other two neighboring octahedra, connected along the  $z$  axis, are not coupled in the same way and can rotate independently. In case of  $\text{NaNbO}_3$ , as shown in

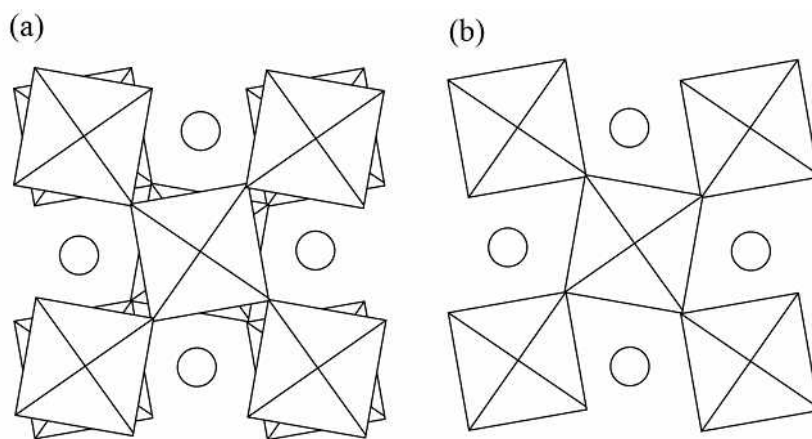


Fig. 4-18 A view looking down the  $z$  axis of two adjacent layers of octahedra for (a) tetragonal  $\text{CaTiO}_3$  and (b) tetragonal  $\text{NaNbO}_3$ . Polyhedral representation symbolizes a metal ion surrounded by six O ions. The round circles represent the M1 ions.

Fig. 4-18 (b), other two neighboring octahedra rotate in the opposite direction of  $\text{CaTiO}_3$ .

The M1 cation coordination for cubic and tetragonal perovskite-type oxides is shown in Fig. 4-19. In cubic phase perovskite-type oxides, as shown in Fig. 4-19 (a), M1 ion is surrounded by 12 oxide ions. The coordination state around M1 ion changes by phase transition from cubic phase to tetragonal phase. In case of  $\text{CaTiO}_3$ , the four closest O ions surround M1 ion in a distorted tetrahedron. On the other hand, in the case of  $\text{NaNbO}_3$ , the closet four ions around M1 ion is rectangular planar instead of distorted tetrahedral. This indicates that the role of M1 ion changes by tilting system.

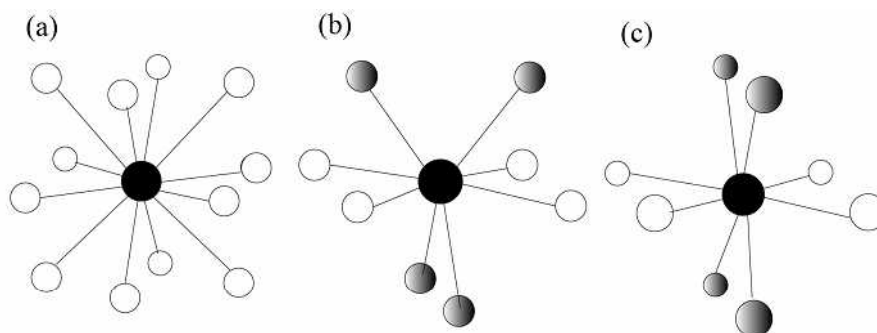


Fig. 4-19 M1 ion coordination for (a) cubic perovskite-type oxide, (b) tetragonal  $\text{CaTiO}_3$  and (c) tetragonal  $\text{NaNbO}_3$ . The filled circles represent M1 ion, the lightly shaded circles represent the closet O ions and the open circles represent the second-neighbor O ions.

Thus, the atomization energy concept allows us to investigate the change of the contribution of each constituent element by phase transition. It is stressed here that the total energy calculation can hardly demonstrate clear changes with the phase transition, and hence the soft phonon mode approach has been commonly used. However, the present approach provides a clue to the understanding of the phase transition in a fundamental manner.

#### 4.3.4 Carbides and nitrides

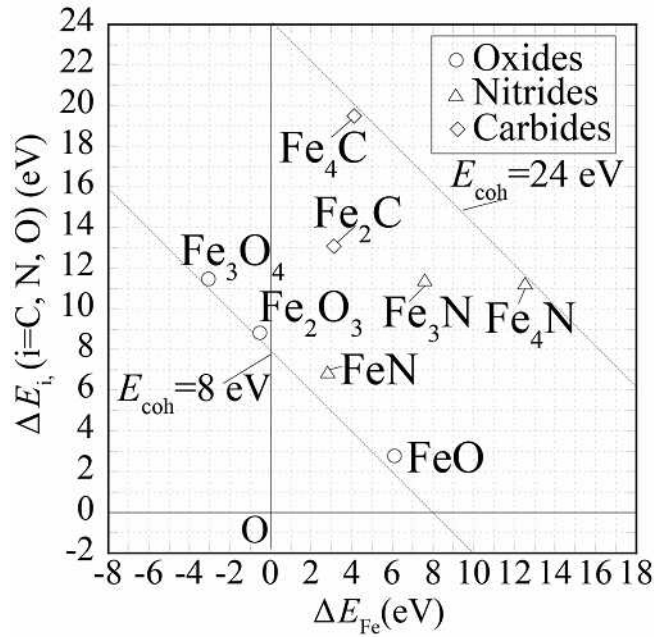


Fig. 4-20 Atomization energy diagram for binary Fe carbides, nitrides and oxides.

Traditionally, it is thought that the ionic interaction is significant in the order, oxides > nitrides > carbides, and the covalent interaction changes in the reverse order, oxides < nitrides < carbides. In fact, according to the Mulliken population analysis, the net charge on O (or N, C) ion normalized by the formal charge changes in the order, FeO(-0.36), Fe<sub>3</sub>O<sub>4</sub>(-0.32), Fe<sub>2</sub>O<sub>3</sub>(-0.30) < Fe<sub>3</sub>N(-0.26), Fe<sub>4</sub>N(-0.24) < Fe<sub>2</sub>C(-0.13), Fe<sub>4</sub>C(-0.12). In this section, for the comparison with the oxides, binary metal carbides and nitrides such as Fe<sub>2</sub>C, Fe<sub>4</sub>C, FeN, Fe<sub>3</sub>N and Fe<sub>4</sub>N are analyzed in view of the atomization energy concept.

The atomization energy diagram for binary Fe carbides and nitrides is shown in Fig. 4-20 together with the result of binary Fe oxides. Binary Fe carbides and nitrides with the higher compositional ratio, M/C or M/N, have the higher cohesive energy compared to that of binary Fe oxides. Also, in all the carbides and nitrides,  $\Delta E_{\text{Fe}}$  is always positive,

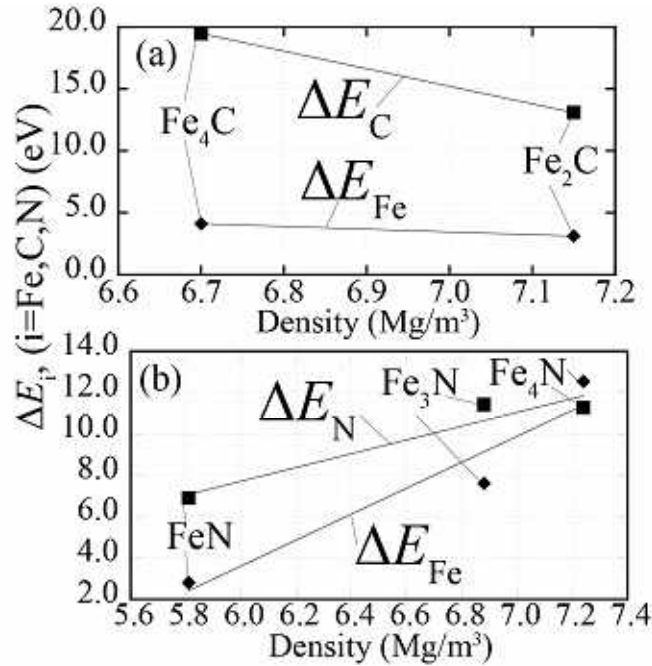


Fig. 4-21 Correlation between atomization energy and density of (a) binary Fe carbides and (b) binary Fe nitrides.

indicating that the strong covalent interactions are operating between M-C, M-N and M-M atoms in carbides and nitrides. This probably causes the high  $\Delta E_{Fe}$  in them.

The correlation between the atomization energy and the density is shown in Fig. 4-21. In binary metal carbides such as  $\text{Fe}_2\text{C}$  and  $\text{Fe}_4\text{C}$ , both  $\Delta E_M$  and  $\Delta E_C$  decrease with increasing density as shown in Fig. 4-21 (a). On the other hand, in binary metal nitrides such as  $\text{FeN}$ ,  $\text{Fe}_3\text{N}$  and  $\text{Fe}_4\text{N}$ , both  $\Delta E_M$  and  $\Delta E_N$  increase with increasing density as shown in Fig. 4-21 (b). Thus, a correction of the atomization energy with the density is different among the binary oxides, carbides and nitrides. As described earlier,  $\Delta E_O$  decreases but  $\Delta E_M$  increases with the density (see Fig. 4-7). This difference may be attributable to the difference in the composition among them. Namely, the compositional ratio of M/O, or M/C or M/N is smaller than unity for oxides, but larger

than unity for the carbides and nitrides. In other words, in addition to the M-C (or N), the M-M interaction becomes more dominant in the carbides and nitrides than in the oxides. Further analysis is performed to confirm this result.

The normalized atomization energy diagram per atom for binary Fe nitrides is shown in Fig. 4-22 (a). On this diagram, the atomization energy  $\Delta E'$  is normalized by the total number of ions in the chemical formula,  $n$ , (e.g.,  $n = 5$  for  $\text{Fe}_4\text{N}$  and  $n = 2$  for  $\text{FeN}$ ). The positions of binary Fe nitrides are aligned along a dot line, as shown in Fig.

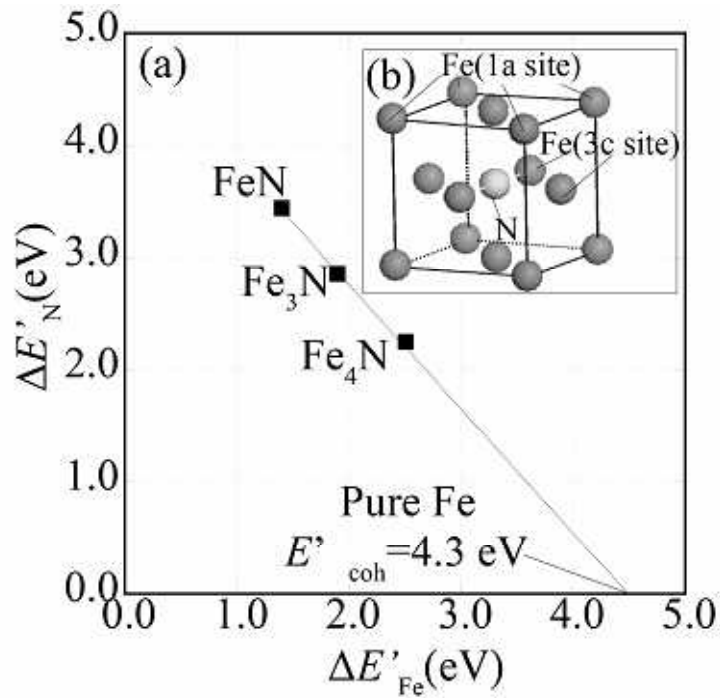


Fig. 4-22 (a) Normalized atomization energy diagram per atom for binary Fe nitrides and (b) crystal structure of  $\text{Fe}_4\text{N}$ .

4-22 (a). On this diagram, the point at the intersection of a dot line and the horizontal axis at  $\Delta E'_N = 0$  falls on the Fe state in pure Fe.

The crystal structure of  $\text{Fe}_4\text{N}$  is shown in Fig. 4-22 (b). In  $\text{Fe}_4\text{N}$ , there are two Fe sites; 1a site and 3c site. The 1a site is located near the Fe site and the 3c site is located near the nitrogen site. The atomization energy of Fe at the 1a site ( $\Delta E'_{\text{Fe}} = 3.9 \text{ eV}$ ) is

found to be higher than that of Fe at the 3c site ( $\Delta E'_{\text{Fe}} = 2.9 \text{ eV}$ ). This indicates clearly that the Fe state is stabilized by the strong interaction between Fe atoms. The Fe ion neighboring N ion is destabilized to some extent due to the Fe-N interaction, but instead the N ion state is probably stabilized through this interaction. There is a trend that the Fe state in these nitrides is stabilized with increasing compositional ratio of Fe/N. As explained earlier, the strong chemical interaction between Fe ions is operating, since nitrides have higher compositional ratios of metal to nitrogen, compared to the oxides.

#### 4.3.5 Atomization energy diagram for hydrides, hydrocarbons, oxides carbides and nitrides.

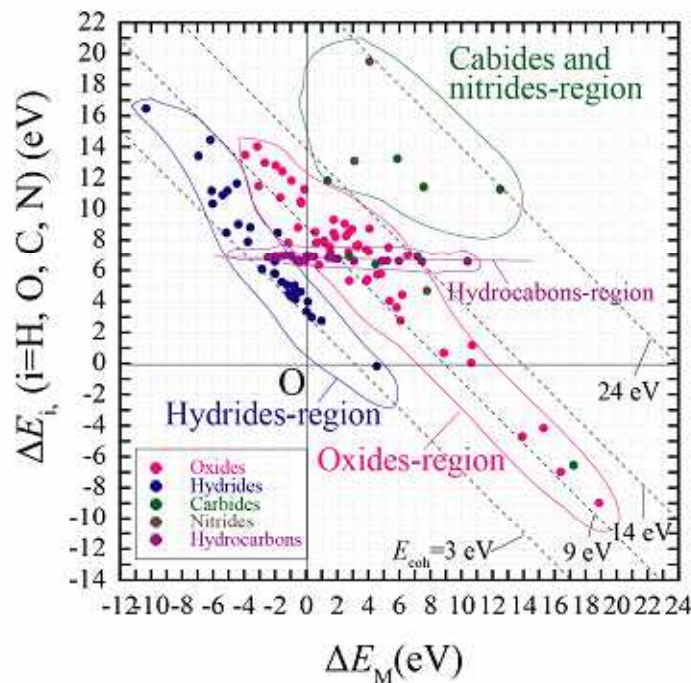


Fig. 4-23 Atomization energy diagram for hydrides, hydrocarbons, oxides, carbides and nitrides.

The atomization energy diagram for hydrides, hydrocarbons, oxides, carbides and nitrides is summarized in Fig. 4-23. Each material has its own existence region in the

diagram. For example,  $E_{\text{coh}}$  lies 3-9 eV for hydrides,  $E_{\text{coh}}$  lies 7-14 eV for oxides, and 10-24 eV for carbides and nitrides. Thus, chemical bond strength changes in the order, hydrides < oxides < carbides, nitrides. The region of the hydrocarbons is extended over the wide range of  $\Delta E_M$  (i.e.,  $M = C$ ).

For oxides and hydrides,  $\Delta E_O$  (or  $\Delta E_H$ ) increases with decreasing  $\Delta E_M$ . For the oxides and hydrides, the  $E_{\text{coh}}$  value shows less change, as compared to the relatively larger change in both  $\Delta E_O$  (or  $\Delta E_H$ ) and  $\Delta E_M$ . In other words, the electronic state of O (or H) ion is adjusted largely depending on M. So, there is a certain energy balance between the M and O (or H) ions in the atomization energy diagram. On the other hand, for hydrocarbons,  $C_mH_n$ ,  $\Delta E_H$  is nearly constant and  $\Delta E_C$  increases with increasing m/n. Thus,  $E_{\text{coh}}$  changes significantly with the molecules. For carbides and nitrides, not only M-C or (M-N) interaction but also M-M interaction is operating owing to the higher compositional ratio of M to C (or N). As a result, an energy balance between M and C (or N) is not seen clearly in the atomization energy diagram.

#### 4.4 Conclusion

Based on the atomization energy concept, the nature of the chemical bond in binary metal oxides and perovskite-type oxides are investigated in view of the local structure, average structure and phase transition. The local ionic arrangements and compositional ratio of metal to oxygen are sensitive to the atomization energy, and the metal state (or oxide ion state) changes with the density of the binary metal oxides. Also, a shared oxide ion appears to be in the more stable state than a non-shared one. Among the corner, edge and face sharing oxide ions in the polyhedron, the edge-shared one is the

most stable in the oxides. This is probably a reason why the oxide ion is often shared by the edge in many oxides.

In the perovskite-type oxides,  $M_1M_2O_3$ , there is an energy balance between  $\Delta E_{M_1}$  and  $\Delta E_{M_2}$ , and the balance changes depending on  $M_1$ . Also, the oxide ion state is formed to be stabilized in  $\text{CaTiO}_3$  (or  $\text{BaTiO}_3$ ) by tilting-type (or displacement-type) phase transition from cubic to tetragonal phase. With the tilting-type phase transition the atomization energies change largely owing probably to the expansion of O-O distance and hence to the reduced the O-O Coulomb repulsive interaction. In addition, the atomization energy appears to reflect the rotation direction of  $\text{MO}_6$  octahedra in perovskite-type oxides. For example, for  $\text{NaNbO}_3$ , by the phase transition cubic to tetragonal phase,  $\text{NbO}_6$  octahedron rotates in the opposite direction as the  $\text{TiO}_6$  octahedron does in  $\text{CaTiO}_3$ . The oxide ion state is stabilized by phase transition from cubic to tetragonal phase. This trend is the reverse trend of  $\text{CaTiO}_3$ . In addition,  $M_1$  (e.g.,  $M_1 = \text{Ca}, \text{Na}$ ) ion plays an important role in the change of oxide ion state by the tilting-type phase transition. For example, for tetragonal  $\text{CaTiO}_3$ , the Ca ion and the closest four oxide ions form a tetrahedron. On the other hand, for tetragonal  $\text{NaNbO}_3$ , the oxide ion is destabilized and Na ion state is stabilized compared to cubic  $\text{NaNbO}_3$ . On the other hand, in case of the displacement-type phase transition (e.g.,  $\text{BaTiO}_3$ ), the changes of the atomization energies with the phase transition are very small.

Thus, the present analysis of the chemical bond based on the atomization energy concept allows us to understand how the materials build up its crystal structure. Also, it will provide us a new tool for investigating the role of the constituent element in materials. Furthermore, by using atomization energy diagram, the nature of the chemical bond in

various materials such as hydrides, hydrocarbons, oxides, carbides and nitrides can be compared with each other in an energy scale.

## REFERENCES

- [1] M. Yoshino, Y. Liu, K. Tatsumi, I. Tanaka, M. Morinaga and H. Adachi, *Solid State Ionics* 162-163 (2003) 127-133.
- [2] S. Miyake, and R. Ueda, *Journal of the Physical Society of Japan*, 2 (1947) 93-97.
- [3] A. Ahtee, M. Ahtee, A. M. Glazer and A. W. Hewat, *Acta Cryst. B* 32 (1976) 3243-3246.
- [4] M. Ahtee, A. M. Glazer and A. W. Hewat, *Acta Cryst. B* 34 (1978) 752-758.
- [5] R. E. Cohen, *Nature* 358 (1992) 136-138.
- [6] R. E. Cohen and H. Krakauer, *Ferroelectrics* 136 (1992) 65-83.
- [7] L. Stixrude and R. E. Cohen, *Nature* 364 (1993) 613-615.
- [8] T. Tohei, A. Kuwabara, T. Yamamoto, F. Oba and I. Tanaka, *Phys. Rev. Lett.* 94 (2005) 035502(1)-035502(4).
- [9] K. Parlinski, Y. Kawazoe and Y. Waseda, *J. Chem. Phys.* 114 (2001) 2395-2400.
- [10] M. Yoshino, H. Yukawa and M. Morinaga, *Mater. Trans.* 45 (2004) 2056-2061.
- [11] W. Kohn and L. J. Sham, *Phys. Rev.* 140 (1965) A1133-A1138.
- [12] J. P. Perdew, K. Burke and Y. Wang, *Phys. Rev. B* 41 (1970) 7892-7895.
- [13] V. Milman, B. Winkler, J. A. White, C. J. Pickard, M. C. Payne, E. V. Akhmatovskaya and R. H. Godby, *Int. J. Quant. Chem.* 77 (2000) 895-910.
- [14] D. Vanderbilt, *Phys. Rev. B* 41 (1990) 7892-7895.
- [15] J. C. Slater, *Phys. Rev.* 81 (1951) 385-390.
- [16] A. D. Becke, *Phys. Rev. A*. 38 (1988) 3098-3100.
- [17] S. H. Vosko, L. Wilk and M. Nusair, *Can. J. Phys.* 58 (1980) 1200-1211.
- [18] C. Lee, W. Yang and R. G.Parr, *Phys. Rev. B*. 37 (1988) 785-789.
- [19] A. Schafer, H. Horn and R. Ahlrichs, *J. Chem. Phys.* 97 (1992) 2571-2577.
- [20] A. Schafer, C. Huber and R. Ahlrichs, *J. Chem. Phys.* 100 (1994) 5829-5835.
- [21] S. Huzinaga, J. Andzelm, M. Klobukowski, E. Radzioandzelm, Y. Sakai, H. Tatewaki, *Gaussian Basis sets for Molecular Calculation*, Elsevier, New York, 1984.
- [22] V. A.Rassolo, J.A. Pople, M. Ratner and T.L. Windus, *J. Chem. Phys.* 109 (1998) 1223-1229.
- [23] W. J. Hehre, R. Ditchfield and J. A. Pople, *J. Chem. Phys.* 56 (1972) 2257-2261.
- [24] K. D. Dobbs and W. J. Hehre, *J. Comput. Chem.* 7 (1986) 359-378.
- [25] H. Nakai, Y. Kurabayashi, M. Katouda and T. Atsumi, *Chem. Phys. Lett.* 438

(2007) 132-138.

[26] H. Nakai, Chem. Phys. Lett. 363 (2002) 73-79.

[27] R. C. Weast, M. J. Astle and W. H. Beyer, CRC Handbook of Chemistry and Physics, A Ready-reference Book of Chemical and Physical Data (84th ed.), CRC Press 2003.

[28] B. J. Kennedy, C. J. Howard and B. C. Chakoumakos, J. Phys. Condens. Mater. 11 (1999) 1479-1488.

[29] X. Liu and R. C. Lieberman, J. Solid State Chem. 20 (1993) 171-175.

[30] G. H. Kwei, A. C. Lawson, S. J. L. Billinge, S. W. Cheong, J. Phys. Chem. 97 (1993) 2368-2377.

[31] J. W. Edwards, R. Speiser, H. L. Johnston, J. Am. Chem. Soc. 73 (1951) 2934-2935.

## Chapter 5 General conclusion

This study aims to calculate the atomization energy instead of using total energy and to understand the chemical bond in hydrides and oxides in an energy scale. For this purpose, geometry optimization is performed by plane-wave pseudopotential method. The energy density analysis (EDA) analyzes of optimized structure under periodic boundary condition (PBC) are carried out to partition the total energy of system into atomic energy densities of constituent elements. Atomization energy is defined by subtracting the atomic energy density from the energy of isolated neutral atom. The results obtained in each chapter are summarized as follows.

In Chapter 1, the background and the purpose of the present study are explained.

In Chapter 2, two calculation methods used in the present study are explained. One is the plane-wave pseudopotential method and the other is the energy density analysis method.

In Chapter 3, an atomization energy diagram, which is obtained by EDA, is constructed for the first time to treat the chemical interactions in hydrides in an energy scale. All the hydrides, such as binary metal hydrides, perovskite-type hydrides, metal hydrides, complex hydrides, and hydrocarbons can be located on this diagram, although there are significant differences in the nature of the chemical bonds among them.

For hydrocarbon,  $C_mH_n$ , the nature of the chemical bond in  $C_mH_n$  can be understood by using the atomization energies,  $\Delta E_C$  and  $\Delta E_H$ , but without using the concept of single or multiple bonds. Also,  $\Delta E_C$  increases linearly with the ratio of the carbon number to

the hydrogen number,  $m/n$ , while  $\Delta E_H$  remains constant. This indicates that the chemical stability of  $C_mH_n$  is dependent only on the  $m/n$  ratio.

For example, for perovskite-type hydrides,  $\text{NaMgH}_3$  is located just in between  $\text{NaH}$  and  $\text{MgH}_2$  in atomization energy diagram. It is evident that  $\text{NaMgH}_3$  inherits the nature of the chemical bond from  $\text{NaH}$  and  $\text{MgH}_2$  to some extent. Also, it is found that M1 and M2 contributions to the cohesive energy of the perovskite-type hydride,  $\text{M1M2H}_3$ , are nearly equal, as long as M1 and M2 are non-transition metal.

For metal hydrides,  $\text{M1M2H}_n$  (e.g., M1 = Ti, M2 = Fe for  $\text{TiFeH}_2$ , M1 = Mg, M2 = Ni for  $\text{Mg}_2\text{NiH}_4$ ), the role of constituent element is clarified by using the atomization energy. By hydrogenation, the atomization energy decreases in both M1 and M2. However, the decrement is more remarkable in  $\Delta E_{M2}$  than in  $\Delta E_{M1}$  owing to the shorter M2-H distance compared to the M1-H distance. As a result, most of the energy of M2 transfers to the hydrogen and the H state becomes very stable.  $\text{TiFeH}_2$  and  $\text{Mg}_2\text{NiH}_4$  are formed by hydrogenation of  $\text{TiFe}$  and  $\text{Mg}_2\text{Ni}$ , respectively. In these compounds, there is a large difference between  $\Delta E_{M1}$  and  $\Delta E_{M2}$ , indicating that both  $\text{TiFe}$  and  $\text{Mg}_2\text{Ni}$  intermetallic compounds have a strong chemical bond between the M1 and M2 atoms. This is a reason why the hydrogenation and dehydrogenation reactions take place smoothly without changing the alloy compositions. Also, it is interesting to note that  $\text{TiFeH}_2$ , which desorbs and absorbs hydrogen at room temperature, has the largest cohesive energy, 8.3 eV, of the metal hydrides.

For complex hydrides,  $\text{M1M2H}_n$ , the H state is stabilized well in compensation for the destabilized M2 state. The order of hydrogen stability agrees with the order of

cohesive energy. The H state in  $\text{Mg}(\text{AlH}_4)_2$  is the least stable among the alanate (Al) - type complex hydrides. Also, the coordination number effect can be understood using an atomization energy concept. For example, the H state is less stable in the six-H coordinated  $\text{Na}_3\text{AlH}_6$  than in the four-H coordinated  $\text{NaAlH}_4$ .

In Chapter 4, based on the atomization energy concept, chemical bond in binary metal oxides and perovskite-type oxides are investigated in view of the local structure, average structure and phase transition as well. The atomization energy reflects the oxides structure such as interionic distances between metal and oxide ions, the coordination number and the sharing state of polyhedra. The oxygen state in binary metal oxides is more stabilized with decreasing interionic distance between metal and oxide ions and also with decreasing the coordination number. When the local ionic arrangements and compositional ratio of metal to oxide ion are similar between oxides, the metal ion state (or oxide ion state) changes with the density of them. One example is  $\text{TiO}_2$ , in which the density is  $3.84 \text{ Mg/m}^3$  for the anatase and  $4.24 \text{ Mg/m}^3$  for the rutile. The Ti ion state becomes stable but the oxide ion state becomes unstable with the density in  $\text{TiO}_2$ . Also, a shared oxide ion between neighboring polyhedra is more stabilized than a non-shared one. It seems most stabilized when the polyhedra are linked together by the edge sharing.

For the perovskite-type oxides,  $\text{M}_1\text{M}_2\text{O}_3$ , there is an energy balance between  $\Delta E_{\text{M}_1}$  and  $\Delta E_{\text{M}_2}$ , and the way for balancing depends on M1. Also, the atomization energy changes with the crystal structure. For example, in  $\text{CaTiO}_3$  (or  $\text{BaTiO}_3$ ) oxide ion state is stabilized by tilting-type (or displacement-type) phase transition from cubic to tetragonal phase. By tilting-type phase transition the atomization energies change

largely owing probably to reduced the O-O Coulomb interaction. Also, for  $\text{NaNbO}_3$ , by phase transition from cubic to tetragonal phase,  $\text{NbO}_6$  octahedron rotates in the opposite direction as  $\text{TiO}_6$  octahedron does in  $\text{CaTiO}_3$ . The oxide ion state in  $\text{NaNbO}_3$  is destabilized by phase transition from cubic to tetragonal phase. This trend of  $\text{NaNbO}_3$  is completely reverse of  $\text{CaTiO}_3$ . Thus, it is found that the atomization energy reflects the rotation direction of  $\text{MO}_6$  octahedra in the perovskite-type oxides. On the other hand, by displacement-type phase transition (e.g.,  $\text{BaTiO}_3$ ), the changes of the atomization energies are very limited.

Furthermore, the atomization energy diagrams are compared among oxides, carbides and nitrides. It is shown that the compositional ratio of M/O or M/C or M/N is very different among them. For example, M/O is smaller than unity, but M/C or M/N is larger than unity. As a result, the M-M interaction becomes dominant in carbides and nitrides. This appears to lead to the higher M state, while keeping the higher C (or N) state.

By using an atomization energy diagram, the nature of the chemical bond in various materials such as hydrides, hydrocarbons, oxides, carbides and nitrides can be analyzed in an energy scale. The present unified approach based on the atomization energy concept will provide us new insight of chemical bond in materials, and hence it will give a new clue to materials design.

## List of Paper Related to the Present Study

### Chapter 3

“A unified approach to the analysis of the chemical bond in hydrides and hydrocarbons”

Y. Shinzato, H. Yukawa, M. Morinaga, T. Baba and H. Nakai

Acta Materialia 55 (2007) 6673-6680.

“Energy density analysis of the chemical bond between atoms in perovskite-type hydrides”

Y. Shinzato, H. Yukawa, M. Morinaga, T. Baba and H. Nakai

Journal of Alloys and Compounds 446-447 (2007) 162-165.

“New Expression of the Chemical Bond in Hydrides Using Atomization Energies”

Y. Shinzato, H. Yukawa, M. Morinaga, T. Baba and H. Nakai

Advances in Quantum Chemistry 54 (2008) 145-160.

### Chapter 4

“New Expression of the Chemical Bond in Perovskite-type Metal Oxides”

Y. Shinzato, Y. Saito, H. Yukawa, M. Morinaga, T. Baba and H. Nakai

Material Science Forum 561-565 (2007) 1823-1826.

“Analysis of Chemical Bond in Metal Oxides Based on the Atomization Energy Concept”

Y. Shinzato, Y. Saito, M. Yoshino, H. Yukawa, M. Morinaga, T. Baba and H. Nakai

To be submitted.

## **Acknowledgments**

I express my thanks to many people who have helped me over this period. Above all, I would like to thank Professor Masahiko Morinaga for supervising and encouraging me throughout my research. In particular, I am indebted to Associate Professor Yoshinori Murata and Assistant Professor Hiroshi Yukawa at Nagoya University for their valuable help and advice. In addition, I would like to thank Professor Hidefumi Asano of Nagoya University and Professor Hiromi Nakai of Waseda University. I will remember my co-workers in this research with great affection. In particular, I am indebted to Dr. Takeshi Baba of Waseda University and Assistant Professor Masahito Yoshino of Nagoya University for their valuable help.

Furthermore, I would like to thank all the staff at the Materials Design Laboratory for providing me such a pleasant place to work. I owe it to Ms. Shoko Samma, who has helped me in many occasions.

I am grateful to the Japan Society for the Promotion of Science and the 21st century COE Program “Nature-Guided Materials Processing” of the Ministry of Education, Culture, Sports, Science and Technology for supporting this research.

Finally I would like to thank my parents and my brother for their unfailing support.

Nagoya, January 2008

Yoshifumi Shinzato